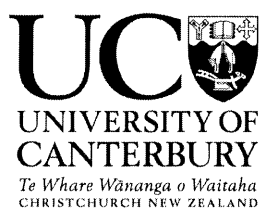


The Onsager heat of transport at the liquid- vapour interface of *p*-tert-butyltoluene



**A thesis completed as the requirement for the
degree of Master of Science in Chemistry**

Georgina Aimee Biggs

2007

University of Canterbury

Abstract

The Onsager heat of transport for *p*-tert-butyltoluene was measured, as part of a series of preliminary experiments towards the determination of the importance of temperature gradients on the air-sea flux of carbon dioxide. The results presented in this thesis imply that the temperature gradient is a major contributor to the magnitude of the air-sea flux.

The heat of transport has been measured for the *p*-tert-butyltoluene system by measuring stationary-state pressure changes for known temperature differences on the vapour side of the interface. At the pressure ranges used the number of mean free paths was always outside the Knudsen zone, but the values of Q^* were approximately 100 % of the latent heat of vaporisation. Departures from linearity of plots of P against ΔT are attributed to temperature jumps at the surface of the dry upper plate.

Both the results taken for *p*-tert-butyltoluene and the earlier results for water from this laboratory fit to a Type III BET isotherm, where the c parameter is not constant. They also reveal the importance of the temperature gradient in determining the value of the thermal accommodation coefficient, and provide a new method of measuring thermal accommodation coefficients for a variety of surfaces and vapours.

Acknowledgements

I would like to take this opportunity to thank my supervisor, Professor L. F. Phillips, for his advice, support and overall interest throughout this project. Many thanks also to Professor C. J. Pursell for all his help and guidance during many of these experiments.

Also to all the members of staff who helped me throughout these experiments, in particular Danny Leonard, Sandy Ferguson, Robert McGregor, Wayne Mackay and Russel Gillard. My gratitude also goes to my lab buddies David Bones and Ronald James for their support and friendship.

Finally I would like to thank my family and friends for all their support and encouragement throughout this year.

Table of Contents

Abstract	i
Acknowledgements	ii
Chapter 1: Introduction	1
1.1 Measurement of the air-sea CO ₂ flux	1
1.2 Derivation	7
1.3 Previous experiments	9
1.4 Scope of this work	20
Chapter 2: Experimental Procedure	21
2.1 Work with the first stainless steel Onsager cell	21
2.1.1 Drying of sample	21
2.1.2 Degassing of sample	21
2.1.3 Distillation of liquid into cell	22
2.1.4 The cell	23
2.1.5 Measurement procedure	25
2.1.6 Analysis	26
2.2 Alternative metal cell	26
2.2.1 Drying of sample	28
2.2.2 Degassing of sample	28
2.2.3 The second cell	29
2.2.4 Measurement procedure	30
2.2.5 Analysis of raw data	31
2.3 Water with N ₂ O vapour above	31
2.3.1 Degassing of sample	31
2.3.2 Introduction of N ₂ O into the cell	32
2.3.3 Diode laser setup	33
2.3.4 Measurement Procedure	36
Chapter 3: Results and Discussion	37
3.1 Analysis of data in terms of the Onsager heat of transport	37

3.2 Temperature jump analysis	44
3.3 Adsorption isotherm analysis.....	46
Chapter 4: Conclusion	58
References	60

Chapter 1: Introduction

1.1 Measurement of the air-sea CO₂ flux

Carbon dioxide, CO₂, is a major contributor to global warming. CO₂ is a “greenhouse” gas, which means that it absorbs infrared radiation emitted from the earth as black body radiation, which in turn warms the atmosphere. The past century has seen the most dramatic release of CO₂ into the atmosphere that has been experienced in the history of the earth. While the concentration has been notably higher at certain periods in the past, there has never been such a vast amount of bound carbon converted to gaseous products over such a short period of time [1]. The scale and pace of recent industrial development around the world have been a major factor influencing the increase of CO₂ to the atmosphere for a variety of reasons, such as the increased combustion of fossil fuels and increased cement production [2]. CO₂ has an estimated atmospheric lifetime of the order of 10 years before it exchanges with the ocean surface or land vegetation [3, 4]. The amount of CO₂ is expected to reach levels double those of the level of the pre-industrial era (about 250 ppm) during this century.

The increase in concentration of various greenhouse gases is of major concern since they contribute to global warming. Global warming is a serious issue; it could lead to problems such as an increase in extreme weather conditions, an increase in the spread of disease and the melting of the ice caps, which in turn would lead to a rise in sea level [4]. Growing concerns over climatic change have heightened the importance of investigations into sources and sinks of greenhouse gases, especially CO₂. Evidence indicates that quite small changes in atmospheric CO₂ can have large effects on planetary climate [4]. This in turn can lead to additional problems, such as the melting of Siberian and Alaskan permafrost, leading to the release of methane, a gas many times more efficient at absorbing infrared radiation than CO₂.

The majority of the carbon that is not locked up in carbonate rocks is contained in the ocean, which contains 15-20 times more carbon than the atmosphere, land vegetation

and soils combined [4]. Therefore, the oceans play a crucial role in the global carbon cycle and in determining the amount of CO₂ in the atmosphere.

The atmosphere and the ocean surface continually exchange CO₂. The top 100-200 m of the ocean are well-mixed; current estimates indicate the oceans are taking up at least a third of all the anthropogenic CO₂ by dissolving it in surface water that then loses contact with the atmosphere due to vertical mixing [5].

The greater amount of CO₂ entering and leaving the oceans also leads to a phenomenon known as ocean acidification. Hydrolysis of CO₂ in seawater increases the hydrogen ion concentration, [H⁺], reducing the pH. It is predicted that the pH will become 0.3 to 0.4 units lower during this century, which corresponds to a 100 to 150 % increase in [H⁺] in the oceans [6]. CO₂ forms carbonic acid when dissolved in water and as the amount of CO₂ released into the atmosphere gradually increases so too does the amount entering into the oceans. The result is a significant decrease in the ratio of carbonate ion concentrations, [CO₃²⁻], to bicarbonate ion concentration, [HCO₃⁻], as can be seen through the following equilibrium:



This acidification damages the animal and plant life inhabiting the oceans, in particular the coral reefs and other organisms that consist, in some part, of calcium carbonate. The decrease in [CO₃²⁻] makes it harder for marine organisms to create biogenic calcium carbonate, CaCO₃ [6].

Concerns about the effects associated with increased atmospheric CO₂ have made accurate measurements of the CO₂ flux between the oceans and the atmosphere increasingly necessary, particularly in the past few decades. Various research groups and organisations have attempted to determine the CO₂ flux, using a variety of methods, with differing results. One such organisation is the Joint Global Ocean Flux Study (JGOFS), which was launched in 1987. It is an international programme with participants from over 20 nations [5]. The central goal for this organisation is to determine regional-to-global

and seasonal-to-interannual fluxes of carbon between the atmosphere, surface ocean and ocean interior, and their sensitivity to climate changes [5].

The air-sea CO₂ flux is often parameterised as:

$$F = ks(p(\text{CO}_{2(\text{water})}) - p(\text{CO}_{2(\text{air})})) = K\Delta p(\text{CO}_2) \quad (2)$$

Where F is the CO₂ flux, k is the transfer velocity (derived from the Schmidt number and the wind speed.)^{*}, s is the solubility, quantified as a function of salinity and temperature, $p(\text{CO}_{2(\text{water})})$ and $p(\text{CO}_{2(\text{air})})$ are the partial pressures of CO₂ in water and air respectively and K is the constant of proportionality, the CO₂ gas exchange coefficient. The CO₂ transfer velocity depends on many factors such as wind speed, bubble entrainment, atmospheric stability and sea state. It is still not well known how particular environmental parameters influence the transfer velocity of CO₂, however it is clear that the gas transfer velocity is a function of wind speed [7]. Current parameterisations almost entirely neglect the role of the air-sea temperature difference, a situation which provides the underlying motivation for the present study.

Currently there are two key methods used for the measurement of the air-sea CO₂ flux, the dual tracer technique and the eddy correlation technique.

The dual tracer technique involves the release of two inert gas tracers into the region or sample being studied. Measurements of the ratio of the two tracers are then used to obtain the gas exchange rate as a function of time [8]. The advantage of this technique is that measurements can be made over fairly short time scales (hours to days), allowing data collection without the need to average over varying environmental conditions [8]. Presently the most common tracers being used are SF₆ and ³He, both of which are volatile. It would be preferable to have one completely non-volatile tracer, as the measurements would enable the direct calculation of the gas exchange rate of the other tracer [8]. However, at present this is not possible, as there is no environmentally acceptable and operationally suitable non-volatile tracer available [9].

^{*} The Schmidt number is a dimensionless number, it is defined as:

$Sc = \nu/D$, where ν is the kinematic viscosity and D is the mass diffusivity

The two tracers are simultaneously released into the ocean [10]. The ratio of the concentrations of the tracers changes with time, as the tracers transfer to the atmosphere at different rates [9]. In a region that is well stirred the ratio changes according to:

$$\left(\frac{1}{R}\right)\frac{dR}{dT} = -\frac{(K_{He} - K_{SF_6})}{H} \quad (3)$$

where K_{He} and K_{SF_6} are the transfer velocities of the two gases across the air-sea interface, H is the water depth and R is the ratio of the concentrations of the tracers [9]. The measurements are adapted to CO_2 using the relationship (4) that links the transfer coefficients of two gases K_i and K_j , to their corresponding Schmidt numbers:

$$\frac{K_i}{K_j} = \left(\frac{Sc_j}{Sc_i}\right)^n \quad n < 0 \quad (4)$$

where Sc_i and Sc_j are the Schmidt numbers associated with the two gases. The value of n is usually assumed to be -0.5 [11]. To compare gas transfer velocities under differing environments they are usually normalised to the Schmidt number of CO_2 at $20^\circ C$ ($Sc = 600$) with $n = -0.5$. The dual tracer method implicitly assumes that both the form of the parameterisation in Equation 2 and the dependence of transfer coefficient on Schmidt number, given in Equation 4, are correct. It represents a first-order improvement on the simple use of Equation 2, in that environmental factors such as the presence or absence of surfactants should roughly cancel from the ratio of K_i to K_j .

In the eddy correlation technique, the differences in concentration of CO₂ in packets of air moving down towards the ocean surface and packets moving away from the ocean surface are measured together with the vertical velocity of each packet. The air moving up from the surface of the ocean has been in contact with the ocean and has lost pollutants, i.e. CO₂, SO₂ etc., via deposition processes [12]. The flux is given by:

$$F(\text{eddy}) = \overline{c'w'} \quad (5)$$

where $F(\text{eddy})$ is the air-sea flux, \bar{c} is the mean gas concentration, \bar{w} is the mean vertical wind velocity and the primes indicate deviations from the mean value [13]. Instantaneous concentrations of CO₂ are measured using a fast-response CO₂/H₂O sensor while a sonic anemometer-thermometer is used to measure three-dimensional wind components and temperature fluctuations [14].

The eddy correlation technique was originally developed for the measurement of terrestrial fluxes [15]. When it is applied to the measurement of the air-sea CO₂ flux significant problems arise, because the flux being measured is at the detection limit of the equipment. This is because a large correction has to be applied due to the interfering effects of water vapour; hence the signal is often smaller than the required correction [8, 15]. The signal strength depends on the air-sea concentration difference and the wind speed [7].

Both techniques have flaws; for example, the dual tracer technique neglects to take into account the effect of the air-sea temperature gradient on the thermodynamic driving force for gas exchange, and assumes that this is provided solely by the CO₂ partial pressure difference (ΔpCO_2 in Equation 2). It also ignores the effect of the 'skin' temperature at the sea surface on the concentration gradient [11, 16]. Eddy correlation values are generally very close to the detection limit of the equipment, they require the use of a large correction, and the data obtained has a large amount of scatter.

Current estimates of the global CO₂ budget do not correspond to the measured values. This is largely believed to be due to the difficulty involved in measuring the air-

sea CO₂ flux. The dual tracer technique and the eddy correlation technique arrive at different values for the flux. Transfer velocity values, k , from eddy correlation measurements were found to be 2 to 2.5 times larger than those measured using the dual tracer method [17]. Some of this discrepancy is likely to be due to the neglect of the coupling, in terms of irreversible thermodynamics, between the heat and gas fluxes at the surface of the ocean in the dual tracer method [16]. Taking the coupling into account introduces a dependence of the air-sea CO₂ flux on the temperature differences across the interface [16]. In order to calculate accurate fluxes, measurements of these temperature differences across the boundary layer must be made.

In previous work by Phillips [16, 18-20] an expression for the steady-state flux of gas through the interface on the basis of irreversible thermodynamics was derived using Onsager's heat of transport, Q^* , which arises from the coupling between the heat and matter fluxes [16, 18, 20, 21]. The theory behind the derivation was sound, but the derivation itself was later found to be incorrect, in part, by Doney [22]. The correct derivation evolved from the use of the dissipation function $T\sigma$ to define the thermodynamic forces. This function quantifies the amount of dissipated energy that could have been used for work in a reversible process [22]. In general terms this function is equal to the sum of a set of products of fluxes, J_i , and forces, X_i .

$$T\sigma = \sum_i J_i X_i \quad (6)$$

A complete derivation is given in Section 1.2 below. The resulting equation describing the heat and mass coupling is:

$$J_i = \frac{-L_{ii}}{\delta} \left(q_i^* \frac{\Delta T}{T} + RT \frac{\Delta P_i}{P_i} \right) \quad (7)$$

The most important aspect of the equation at this point is the fact that the equation shows that the gas flux is affected by both the partial pressure gradient and the temperature gradient, the second of which has previously been ignored in the measurement of air-sea CO₂ fluxes.

1.2 Derivation

Q^* is defined as the Onsager heat of transport. It is the amount of heat absorbed and liberated as a molecule passes from one side of a system through a barrier into the other side of the system. In this case the interface is more like a one-sided membrane as it is not obvious that the second part of the process actually occurs. However, the alternative definition, that Q^* is the amount of excess heat transferred per mole of gas flux in the absence of a temperature gradient is still applicable [23]. A simple equation, Equation 30, for the determination of Q^* can be derived in the following way:

We have a system with two simple fluxes, the heat flux:

$$J_1 = L_{11}X_1 + L_{12}X_2 \quad (8)$$

and the flux of matter:

$$J_2 = L_{21}X_1 + L_{22}X_2 \quad (9)$$

L_{11} and L_{22} are related to the thermal conductivity and diffusion coefficient for the boundary layer, respectively. L_{12} and L_{21} represent coupling coefficients between the two flows. X_1 and X_2 represent the appropriate forces, proportional to the temperature gradient and the gradient of potential, respectively [24]. We can prove that $L_{12} = L_{21}$ as follows:

$$T\sigma = \sum_i J_i X_i \quad (10)$$

becomes

$$T\sigma = J_1 X_1 + J_2 X_2 \quad (11)$$

or

$$T\sigma = L_{11}X_1^2 + L_{12}X_1X_2 + L_{21}X_1X_2 + L_{22}X_2^2 \quad (12)$$

In a system at equilibrium the dissipation is zero. In a stationary state, where one of the fluxes, J_1 say, is zero, the force X_1 adjusts itself so that the dissipation takes a minimum value with respect to this variable. Differentiation of (12) gives

$$\frac{\partial(T\sigma)}{\partial X_i} = 2L_{11}X_1 + L_{12}X_2 + L_{21}X_2 \quad (13)$$

In the stationary state $\frac{\partial(T\sigma)}{\partial X_i} = 0$, because the entropy of production will be at a minimum.

Thus

$$0 = J_1 = L_{11}X_1 + L_{12}X_2 \quad (14)$$

$$L_{11}X_1 = -L_{12}X_2 \quad (15)$$

Substituting this into Equation 13 gives:

$$\frac{\partial(T\sigma)}{\partial X_i} = L_{21}X_2 - L_{12}X_2 = 0 \quad (16)$$

where X_2 is arbitrary. Therefore $L_{12}=L_{21}$.

If Q^* is the heat that travels per unit flux of matter, then we can write:

$$J_1 = L_{11}X_1 + Q^*J_2 \quad (17)$$

In a state where there is no temperature gradient, so that $X_1=0$ we have:

$$J_1 = L_{12}X_2 = Q^*J_2 \quad (18)$$

$$J_2 = L_{22}X_2 \quad (19)$$

Substituting (19) into (18) gives:

$$L_{12}X_2 = Q^*L_{22}X_2 \quad (20)$$

or

$$L_{12} = Q^*L_{22} = L_{21} \quad (21)$$

Substituting back into (9):

$$J_2 = Q^*L_{22}X_1 + L_{22}X_2 \quad (22)$$

$$J_2 = L_{22}(Q^*X_1 + X_2) \quad (23)$$

X_1 is given by:

$$X_1 = -\frac{1}{T} \text{grad}(T) = -\frac{dT}{Tdx} \quad (24)$$

(taken from Denbigh, *The Thermodynamics of the Steady State* [24]) and X_2 similarly by:

$$X_2 = -T \text{grad}\left(\frac{\mu}{T}\right) \quad (25)$$

Where μ is the chemical potential, given by

$$\mu = RT \ln(P) \quad (26)$$

so that

$$X_2 = -RT \frac{dP}{Pdx} \quad (27)$$

By substituting the two driving forces (X_1 and X_2) into Equation 23:

$$J_2 = -L_{22} \left(Q^* \frac{\Delta T}{T\delta} + RT \frac{\Delta P}{P\delta} \right) \quad (28)$$

dx is replaced by δ , which is distance over which change in T occurs. Rearrangement of Equation 28 gives the gas-flux equation:

$$J_2 = -\frac{L_{22}}{\delta} \left(\frac{Q^*}{RT} \frac{\Delta T}{T} + \frac{\Delta P}{P} \right) \quad (29)$$

(where L_{22} differs from Onsager's L_{22} by a factor of RT). During the experiment, the liquid-vapour interface will be allowed to come to a stationary state with $J_2 = 0$, so (29) can be rearranged to give:

$$\frac{Q^*}{RT} = -\frac{\Delta P}{P} \frac{T}{\Delta T} \quad (30)$$

Equation 30 is the desired result. Hence, by measuring steady state pressure differences produced by known temperature differences over a small distance on the vapour side of the interface, we can determine Q^* [23].

1.3 Previous experiments

Similar experiments of this nature have been done in the past. Examples are the experiments done by K. G. Denbigh. Denbigh took two vessels containing a gas and separated them via a rubber membrane. In particular, experiments were carried out investigating the passage of hydrogen, nitrogen and carbon dioxide through a rubber membrane [25]. The two vessels were maintained at slightly different temperatures, with a temperature difference on the order of 10 °C. It was found that the gas passed through the membrane until a stationary pressure was obtained, which prevented any further gas flow. The heat of transport could be positive or negative; typical values of $|Q^*|$ were of the order of 1 kJ mol⁻¹.

Similar experiments by Wirtz and Alexander in 1950 involved two samples of water separated by a permeable membrane, where the pressure difference at equilibrium was measured [26]. The results were different with different membranes: for instance with cellulose-based membranes the effect ($\Delta P/\Delta T$) was negative while for baked clay there was no effect and for goldbeater's skin it was positive. They found that the heat of transfer was of the order of 5 J mol^{-1} [26].

Experiments done more recently by the research group of Professor Leon Phillips at Canterbury University involve a liquid-vapour interface and result in much larger values of Q^* . Measurements of the heat of transport at the interface have been carried out with aniline, *n*-heptanol, sulfuric acid, glycerol-water mixtures and most recently water and ice [23, 27-30]. The Q^* values were all found to be negative, and tended towards the latent heat of vaporisation in magnitude, as n_λ , the number of mean free paths in the vapour gap, tended towards zero [23, 29]. The vapour gap itself is the gap between the liquid surface and the upper plate of the cell, as shall be described in detail in Section 2. Figure 1 shows the dependence of the magnitude of Q^* for *n*-heptanol on n_λ [31]. The largest measured Q^* value was 88 % of the latent heat of vaporisation, which supports the idea that the important part of the temperature gradient is located in the Knudsen layer [31].

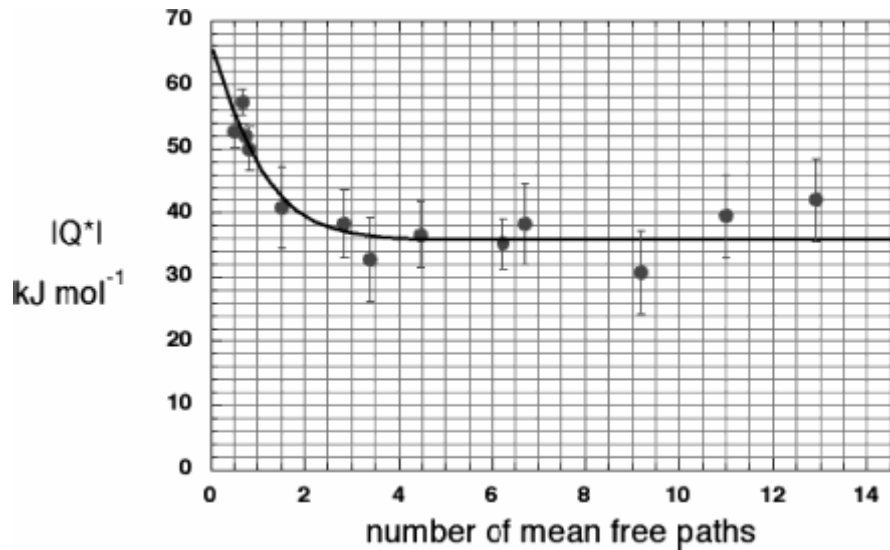


Figure 1: Variation of the measured heat of transport for *n*-heptanol with the number of mean free paths in the gap above the liquid [32].

The Knudsen layer is a region next to the surface of the liquid where molecules travelling towards the surface can have a different velocity from molecules moving away from the surface, that is, the region approximately from $n_\lambda = 0$ to $n_\lambda = 2$ [33, 34]. Within the Knudsen layer there is a significant temperature gradient. Figure 1 shows that the value of Q^* decreases as n_λ increases and once outside the Knudsen layer (approximately when n_λ equals two) the value of Q^* appears to level off to a constant value which is still a significant portion of the latent heat of vaporisation, ΔH_{vap} . This indicates that, even outside the Knudsen layer, a significant temperature effect exists. The temperature gradient across the Knudsen layer has a major effect on the flux of matter through the liquid-vapour interface [35].

After initial experiments with aniline [23] had established the existence of large, negative heats of transport at the liquid-vapour interface, *n*-heptanol was studied because it had a low triple point vapour pressure. The low triple point vapour pressure allowed for the measurement of Q^* values for δ values less than one mean free path, so measurements of P versus ΔT for *n*-heptanol could be performed at very low pressures [29] and values of $|Q^*|$ amounting to more than 80% of the heat of vaporisation were obtained.

Next sulfuric acid-water and the glycerol-water mixture were chosen in order to see how binary mixtures compared to the one-component systems. Previously results could not be obtained for the one-component systems at negative ΔT values because condensation on the upper plate prevented a steady state from being established [29]. However, two component systems no longer had this problem, so Q^* values could be obtained at negative ΔT values for the binary mixtures. Sulfuric acid-water and glycerol-water were interesting to compare because they differed markedly in the extent and strength of hydrate formation.

Values of Q^* for sulfuric acid decreased, in terms of the absolute value, with the decrease in the number of mean free paths in the vapour gap due to the reduction in

vapour pressure of the mixture with increasing acid concentration. This effect was attributed to formation of compounds [27]. In contrast to the sulfuric acid results the glycerol-water plot, followed a similar relationship to the one component systems (i.e. aniline, Figure 1) with no fall off of Q^* at high glycerol concentrations [28].

Since the heat of transport for a hydrocarbon had not been measured previously, comparison with the previous one-component systems could yield more clues to the nature of the gas-liquid interface. *p*-tert-butyltoluene (Figure 2) was chosen as the liquid for the present study because it had similar vapour pressure values to those of *n*-heptanol. The upper limit of vapour pressure was restricted by the apparatus, which uses an MKS Baratron pressure gauge with a range of 0 to 0.25 Torr. The enthalpy of vaporisation, ΔH_{vap} , for *n*-heptanol is approximately 66.81 kJ mol⁻¹ and for *p*-tert-butyltoluene it is approximately 51.8 kJmol⁻¹ (calculated from the temperature dependence of vapour pressure, using data from the Handbook of Chemistry and Physics).

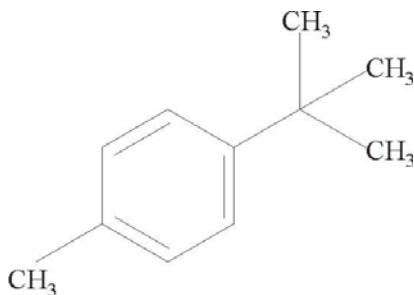


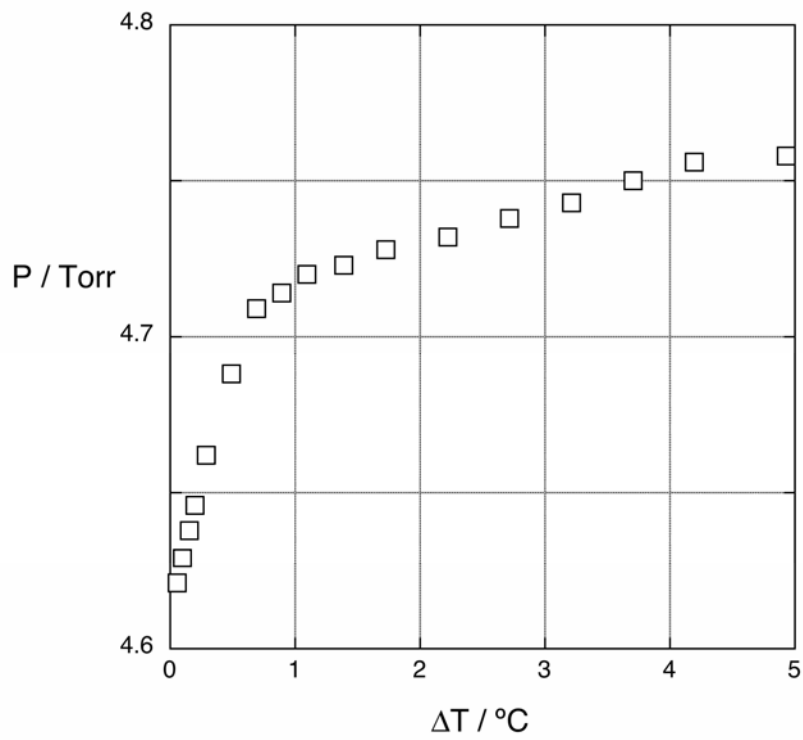
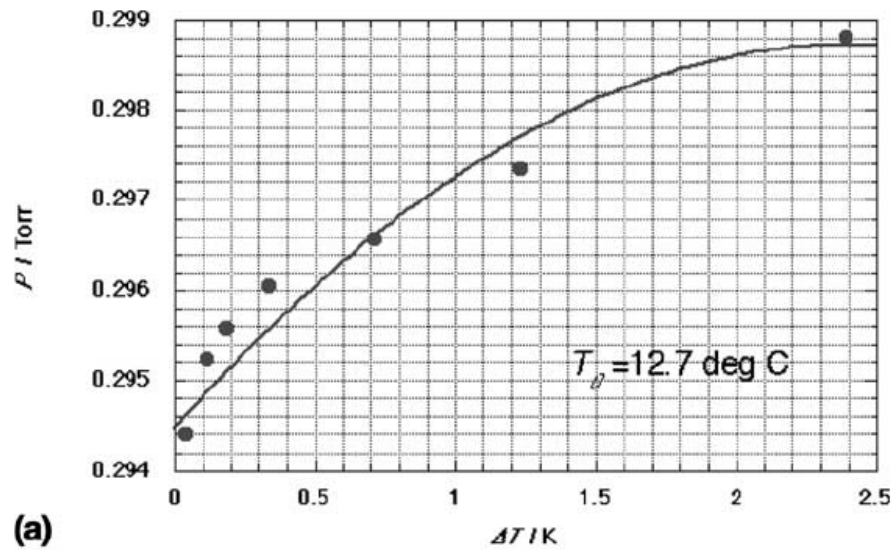
Figure 2: Chemical structure of *p*-tert-butyltoluene.

The most recent experiments were performed with water in a stainless steel cell. Q^* values were again negative and found to be constant at -24.3 ± 3.6 kJ mol⁻¹ over the pressure range 4 to 9.5 Torr [34]. The Q^* values obtained for water were all at large numbers of mean free paths, between the range 200 to 800. The results extended our previous observation that Q^* is independent of pressure when the vapour gap is significantly larger than the mean free path [30].

Equation 30 implies that there should be a linear dependence of ΔP on ΔT . However, deviations from linearity were found for the single component liquids but not for water vapour on sulfuric acid or glycerol. Previously these deviations were attributed

to the possibility that the glass used to make the apparatus was a fairly poor conductor of heat, so horizontal temperature gradients could have existed in the cell. These gradients could have created unwanted gas-phase circulation and turbulence [23]. Further experiments carried out on *n*-heptanol in a stainless steel cell disproved this hypothesis, as the deviations still occurred. The more recent results involving water in a stainless steel cell suggested that these deviations are due to gas-kinetic temperature jumps at the surface of the dry upper plate[30, 34]. The temperature jump is a result of inefficient exchange between the translational energy of gas molecules and the lattice vibrational energy of the solid material with which the molecules collide. The linearity of the results for the two-component systems could be explained by the glass surface being moistened by the water or, possibly, by the adsorption of a small amount of the relatively involatile component, sulfuric acid or glycerol, which would retain a layer of adsorbed water molecules. The thermal accommodation coefficient of water vapour on water is known to be close to unity, so this would result in a negligible temperature jump at the upper plate.

The initial experiments carried out with aniline and *n*-heptanol had resulted in plots which often appeared to have a definite curvature, as can be seen in Figure 3(a). Later experiments with *n*-heptanol and the more recent experiments with pure water have indicated that the curvature is more often a knee with two separate linear portions on either side. Figure 3(b) is a typical plot for the variation in pressure with ΔT over water, showing two distinct linear portions and a pronounced knee when ΔT is approximately 0.5 to 0.8 °C.



(b)
Figure 3: (a) A typical plot of pressure versus temperature change for aniline [23]. (b) A typical plot of pressure versus temperature change for water at 0 °C [30].

During the experiment, as the difference in temperatures of the two plates was decreased, it was observed that the abrupt change in slope, Figure 3(b), occurred at the temperature difference where condensation began to appear on the upper plate [30]. This implied that the steep linear section at low ΔT values corresponded to a wet surface and that the linear portion at higher ΔT values corresponded to a dry surface. (This sort of paradoxical behaviour, with the distillation of a cool liquid onto a warmer surface, was first observed in the experiments conducted on aniline [36] and can be understood as a consequence of Equation 29.)

Experiments carried out starting with the plates equal in temperature and working up towards larger temperature differences gave results in which the initial steep gradient in the P versus ΔT plot continued up to larger ΔT values than was observed for results from measurements with a decreasing temperature difference, as can be seen in Figure 4. This supports the idea of a gradual reduction in the temperature jump due to the adsorption of water onto the upper plate in Figure 3(b); when starting from $\Delta T = 0$ and working up to larger ΔT values, the measurements were taken without waiting sufficiently long for all the water to desorb from the upper plate [30]. Therefore the initial slope was maintained for longer. When all the adsorbed water had evaporated away the pressure dropped down again to approach the expected linear curve of low gradient that would have been obtained had the measurements been taken starting with a dry surface.

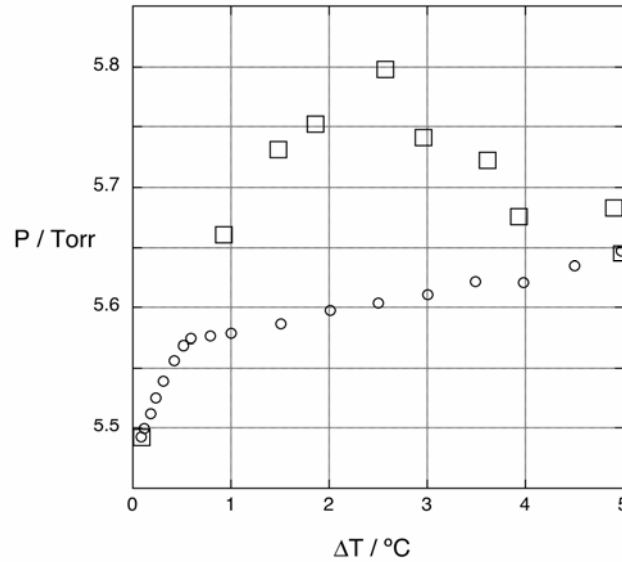


Figure 4: A plot of pressure versus temperature changes for water at 2.5 °C. The circles indicate measurements taken working from large ΔT values down to $\Delta T = 0$, the squares indicate measurements taken working from the opposite direction [30].

The gas-kinetic theory of temperature jumps provides a more detailed view of the gaseous side of the interface [34]. The temperature jump model assumes that there is a heat source at a large distance from the surface that causes a constant long-range temperature gradient away from the surface [37]. The vapour can be described as being bounded by a solid surface with temperature T_W , the temperature at the wall. Figure 5 shows the temperature jump as the quantity $T_K - T_W$, where T_K represents the temperature the gas would have at the wall if the temperature profile had not deviated from linearity [38]. The gas-phase temperature profile can be described by:

$$T(\tau) = \kappa[\zeta + \tau + p(\tau)] \quad (31)$$

where $T(\tau)$ is the temperature difference from the wall temperature, T_W , κ is the long range temperature gradient, ζ is the temperature jump coefficient, which measures the tendency of the gas to have a different temperature from that of the wall [39], τ is the distance from the wall measured in mean free paths and $p(\tau)$ represents the perturbing effect of the wall on the Maxwell-Boltzmann velocity distribution within the Knudsen zone [34]. $T(\tau)$ is actually a dimensionless temperature, which is obtained by dividing the

actual temperature values by a reference temperature that is usually chosen in order to make the slope κ equal to 1, for convenience [30, 34].

Of the molecules striking the wall a fraction, α , become temporarily adsorbed, undergo energy exchange, and later return to the gas, where α is the thermal accommodation coefficient corresponding to the fraction of heat transferred between the surface and the molecule. For water molecules striking a wet surface the accommodation coefficient is 1 [40].

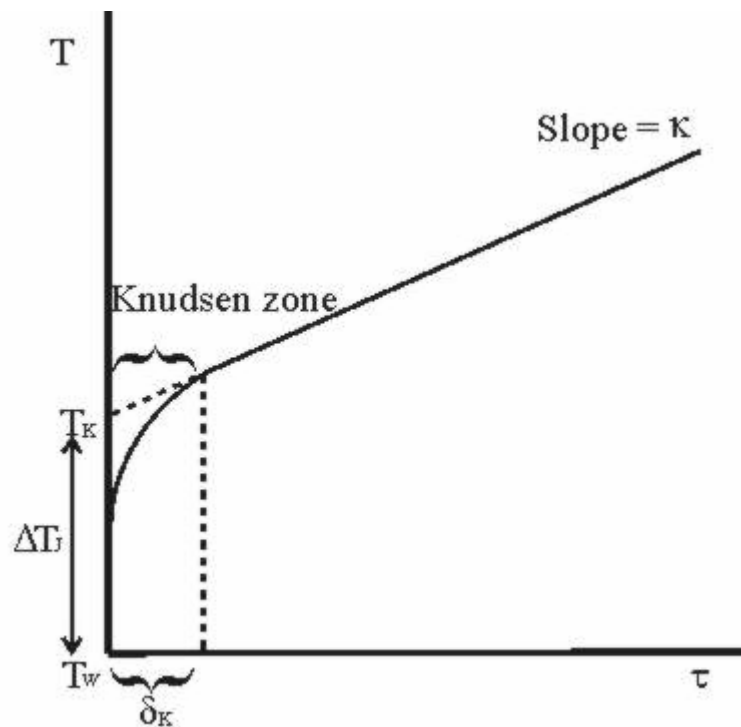


Figure 5: Gas phase temperature profile adjacent to a wall or liquid surface [34, 38].

The symbol δ_K indicates the thickness of the Knudsen zone. Plots of the results for water were analysed as in the diagram shown in Figure 6.

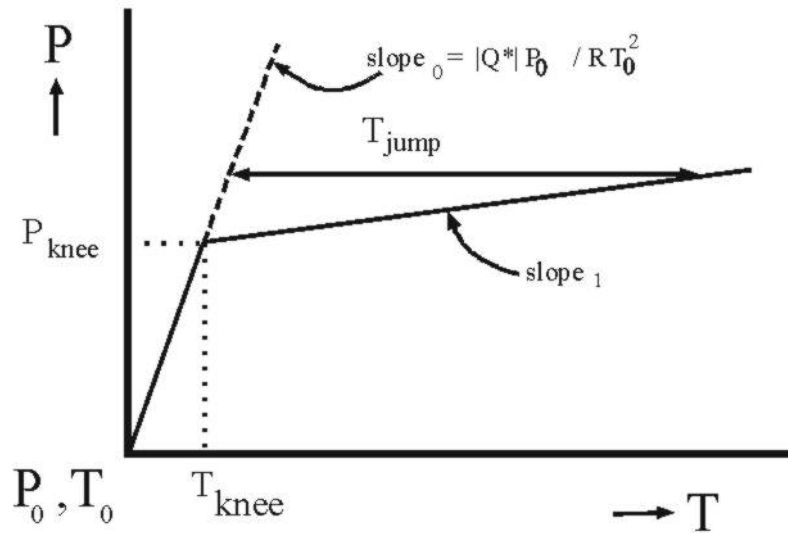


Figure 6: Schematic of the system used to determine Q^* and the values of T_{jump} from plots such as the one seen in Figure 3(b) [30].

Figure 6 shows the basic shape of the results obtained from the experiments carried out on water. The dashed line, which depicts the continuation of the initial linear slope, indicates the temperature of the vapour adjacent to the wall. The solid line labelled $slope_1$ follows the actual temperature of the upper plate. The dashed line shows what would have been observed in the absence of a temperature jump. Hence the temperature jumps, T_{jump} , can be calculated by subtracting the temperature that would have occurred, had the initial slope, $slope_0$ in Figure 6, been followed, from the temperature actually applied, along the line marked $slope_1$.

Plotting data from super-cooled water, a new ice surface and an old ice surface, all at $-2\text{ }^\circ\text{C}$, resulted in three distinct plots, shown in Figure 7. However, when the temperature jumps were plotted against ΔT the relationships for each system were almost identical (Figure 8). This supports the theory that the deviations are due to effects occurring at the upper stainless steel plate.

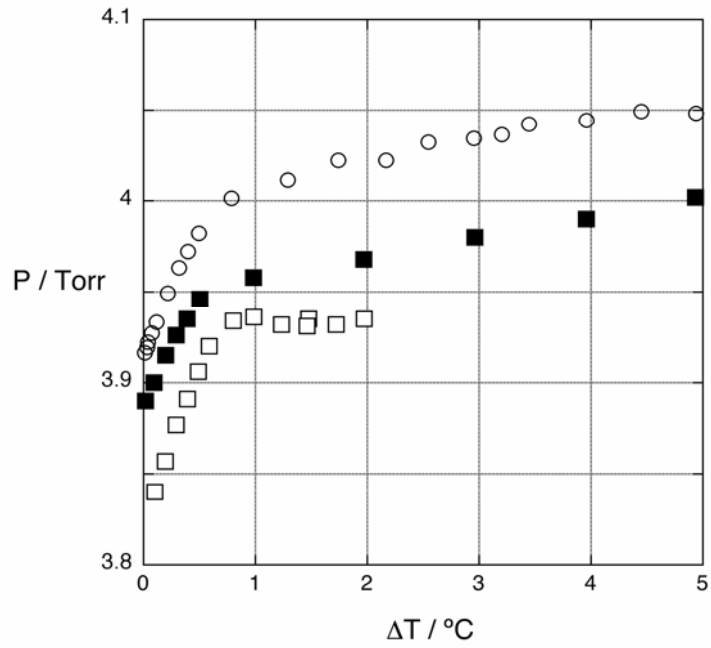


Figure 7: Plots of pressure versus the temperature change for water at -2°C (open circles), a new ice surface (filled squares), and an old ice surface (unfilled squares) [30].

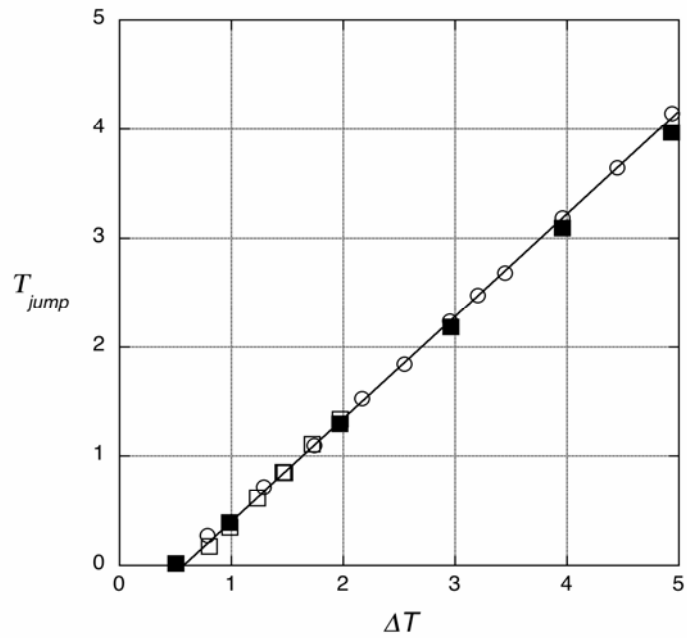


Figure 8: Temperature jumps obtained from the plots. (Open circles: water. Filled squares: new ice. Unfilled squares: old ice.) [30]

1.4 Scope of this work

The present experiment was undertaken to determine whether or not a hydrocarbon would exhibit similar results to the previous experiments of this type. The results were to some extent unexpected, because extreme deviations from linearity were observed, and the heat of transport was always a major fraction of the heat of vaporisation. The resulting data was analysed in a variety of ways. A second set of experiments aimed to measure gas pressure versus the applied temperature difference for N₂O vapour over water, using an infrared diode laser to monitor the N₂O concentration. These experiments were not completed owing to time constraints and the need to purchase a new diode for the required N₂O mode.

Chapter 2 provides a detailed description of the equipment used and the experimental procedures. Experiments on *p*-tert-butyltoluene were carried out in two different stainless steel cells, the initial cell not having a temperature regulating system with the required sensitivity and stability for the small pressure differences being measured. The experimental procedure for the experiments on N₂O is also included in this chapter, but no results can be presented.

Chapter 3 details the results obtained for the experiments done on *p*-tert-butyltoluene in terms of the Onsager heat of transport, followed by analysis of the results with respect to temperature jumps and thermal accommodation coefficients. Analyses of the thermal accommodation coefficients in terms of BET adsorption isotherms are also included in this chapter. Chapter 4 contains the conclusions and an outline for further work that could be undertaken.

Chapter 2: Experimental Procedure

2.1 Work with the first stainless steel Onsager cell

2.1.1 Drying of sample

The initial step in the experimental procedure was to dry the liquid sample, *p*-tert-butyltoluene with calcium hydride. The sample was placed into a round-bottom flask and the calcium hydride added in small quantities until the sample was completely dry. The sample was dry when excess calcium hydride would move freely in the liquid when the flask was swirled. The liquid was then decanted off into another round-bottom flask, from which it was distilled into a degassing chamber connected up to the main vacuum system. The vacuum system consisted of an oil diffusion pump backed by a rotary pump, and isolated by two cold traps.

2.1.2 Degassing of sample

Once the sample was in the degassing chamber, a series of freeze-pump-thaw-boil cycles were performed on the liquid in order to remove any dissolved gases. The chamber was immersed in liquid nitrogen to freeze the sample. Once the liquid had frozen, the chamber was opened up to vacuum to pump off any gases remaining in the chamber. After several minutes the chamber was closed off again, the liquid nitrogen was removed, and the sample left to thaw before being heated to boiling temperature with a hot-air gun (a commercial paint-stripper). This boiling process released any dissolved gases so that they could be removed in the next degassing cycle. The cycle was repeated for two cycles after the liquid was degassed to such an extent that when the frozen sample was opened to vacuum the pressure no longer rose.

2.1.3 Distillation of liquid into cell

Once degassed the sample was ready to be distilled into the cell. This involved boiling the liquid until it had distilled into both the cell and the liquid level adjuster, Figure 9. The liquid was distilled until it could be seen on the bottom plate of the cell.

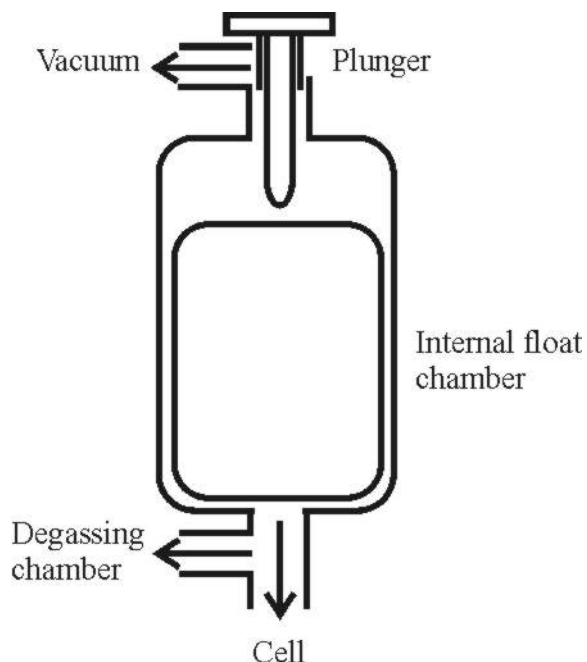


Figure 9: Liquid level adjuster.

At this point, the level of the liquid could be controlled via the liquid level adjuster, as shown in Figure 9. The adjuster contained an internal float chamber, which was a hollow glass cylinder located in the middle of the adjuster. The float had a small depression in the top, which was where the plunger made contact. The plunger was simply a stopcock with an elongated end. When the plunger was screwed down, it drove the chamber down against the liquid below. This altered the pressure on the liquid and hence forced it into the cell until it was level once more. Liquid was sent into the adjuster whilst the plunger was well above the chamber, and once liquid began to appear in the cell the plunger was manoeuvred down onto the chamber forcing liquid into the cell. The liquid level could be adjusted to within 0.1 mm by altering the depth of the plunger in the internal float chamber. It was important not to force too much liquid into the cell because it could

cover the plate and spill over the lip of the plate, becoming trapped between the lip and the glass tubing, as shown by G_{inner} and the lip in Figure 10, surrounding the central compartment of the cell, from where it could not be removed.

2.1.4 The cell

Figure 10 shows the metal cell used initially for the experiments with *p*-tert-butyltoluene.

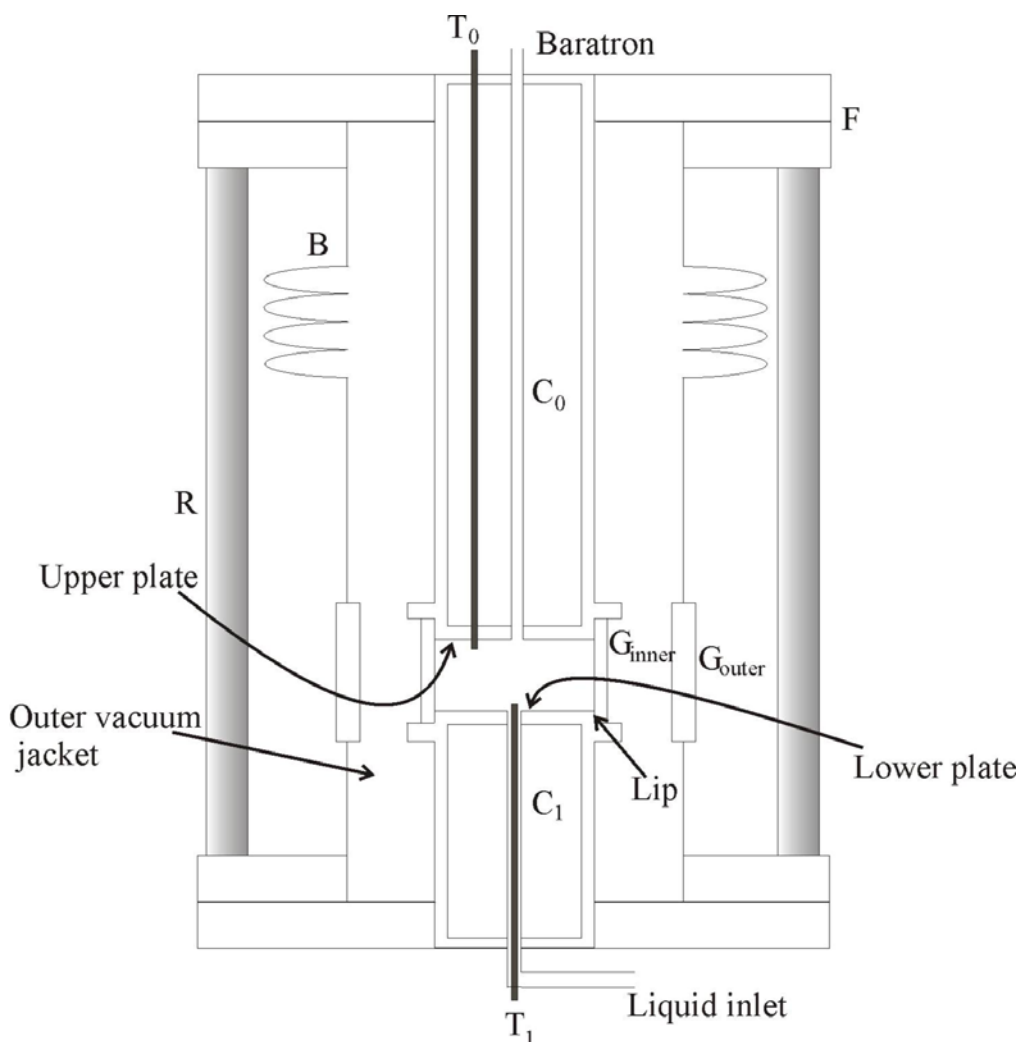


Figure 10: Diagram of the stainless steel cell [29].

The outer component of the cell consists of four stainless steel rods, R, and stainless steel Conflat flanges, F. The middle section is made up of stainless steel bellows, B, and a

length of glass tubing, G_{outer} , which, when combined with the bellows forms an outer vacuum jacket. The central portion consists of three distinct sections. C_0 and C_1 are temperature-regulating compartments. Between them is G_{inner} , another length of glass tubing. The inner length of glass tubing butts against Buna-n gaskets at the top and the bottom to isolate the central liquid compartment from the vacuum jacket. The central liquid compartment consists of two plates; the lower plate is where the liquid is located and the upper plate sits 4mm above the liquid surface.

Ethanol is pumped through compartments C_0 and C_1 via a temperature controlled Julabo ME circulating cryostat. T_0 and T_1 indicate tubes containing PT100 platinum-resistance thermometers. The thermometers are connected to a Tinsley series 5885 interface, which gives a readout of the temperature of each plate at intervals of 3.6 seconds. The computer runs a QuickBasic program, written by Professor Leon Phillips, which reads the temperature via an RS232 connection and displays it, along with the pressure. It also simultaneously plots the temperature of both plates during the experiment allowing observation of their stability. The program also controls the individual temperatures of the two plates, as it contains a temperature-regulating routine, which controls a heater located directly in the flow of ethanol leading into C_0 and another heater located in the flow leading into C_1 . Hence, the Julabo bath was used to bring the general temperature towards a certain point and then the QuickBasic program was used to set and regulate the precise temperatures required for each experiment.

An MKS Baratron type 627B pressure transducer with a range of 0 to 0.25 Torr was used to measure the pressure. The data was collected via a PR4000F 2 channel power supply (with readout for flow and pressure) and the pressure was plotted via the QuickBasic program as a running average of ten points.

2.1.5 Measurement procedure

Q^* was obtained via the measurement of steady state pressure differences for known temperature differences (see Equation 30). ΔT in Equation 30 is the difference in temperature between the vapour, at the upper plate, and the temperature at the surface of the liquid. T is the temperature of the liquid, which remains constant, and P is the vapour pressure when both plates are equal in temperature, i.e. when ΔT equals zero. ΔP is the difference in pressures of the vapour and the pressure obtained when ΔT equals zero. Throughout the experiment values were obtained for all these quantities in order to calculate Q^* .

Before an experimental run was started the sample was allowed to reach a steady state. In practice this required leaving the circulating cryostat on overnight in order to maintain the liquid at an approximate temperature ready to restart the experiment in the morning.

The lower plate was kept at a specific temperature throughout each run. The temperature of the upper plate would be initially 5 °C above the temperature of the lower plate. The temperature of the upper plate was reduced in steps of 0.5 °C until the temperature of the upper plate was approximately 1 °C above that of the lower plate. From this point, the steps were reduced to approximately 0.1 °C apart until the two plates were the same temperature. For each step, the temperature of each plate and the pressure were measured once they were stable. Normally it would take at least 20 minutes after each temperature alteration for the temperatures and the pressure to stabilise.

The temperature of the bottom plate could be maintained to within ± 0.05 °C, while the temperature of the upper plate was only maintained to within ± 0.1 °C of the target value, as the vapour pressure was less sensitive to alterations in the upper plate temperature compared to alterations in the lower plate temperature. Runs were repeated at least three times for the same temperature of the lower plate. A run would then be conducted in reverse, that is starting from $\Delta T = 0$ and working up towards $\Delta T = 5$. The

calculated values of Q^* for each temperature had to agree three times before the reverse run was conducted. This entire procedure was completed for three different temperatures of the lower plate: at 2, 0 and -5 °C.

2.1.6 Analysis

The data was manipulated manually using Equation 30 to calculate Q^* . This involved plotting P against ΔT , which resulted in a linear fit with a slope of $\Delta P/\Delta T$ and an intercept of P_0 , the pressure when ΔT is zero. However, the results obtained using this cell were inconsistent and unreliable. This may have been due to several factors. Liquid from previous experiments using *n*-heptanol had become trapped between the lip of the lower plate and the surrounding glass and could not be removed, which may have interfered with the measured vapour pressure. The very small scale of the pressure measurements limited the sensitivity of the experiments. Also, the temperature-regulating system of the cell was not good enough; a much more precise regulating system was needed.

2.2 Alternative metal cell

To address the problems of trapped liquid and insufficiently sensitive pressure measurements, the new metal cell constructed for the water and ice measurements was used to measure heat of transport values for *p*-tert-butyltoluene (Figures 11 and 12).

Figure 11 shows the cell separated into four pieces. These pieces all slot together to form the cell shown in Figure 12.

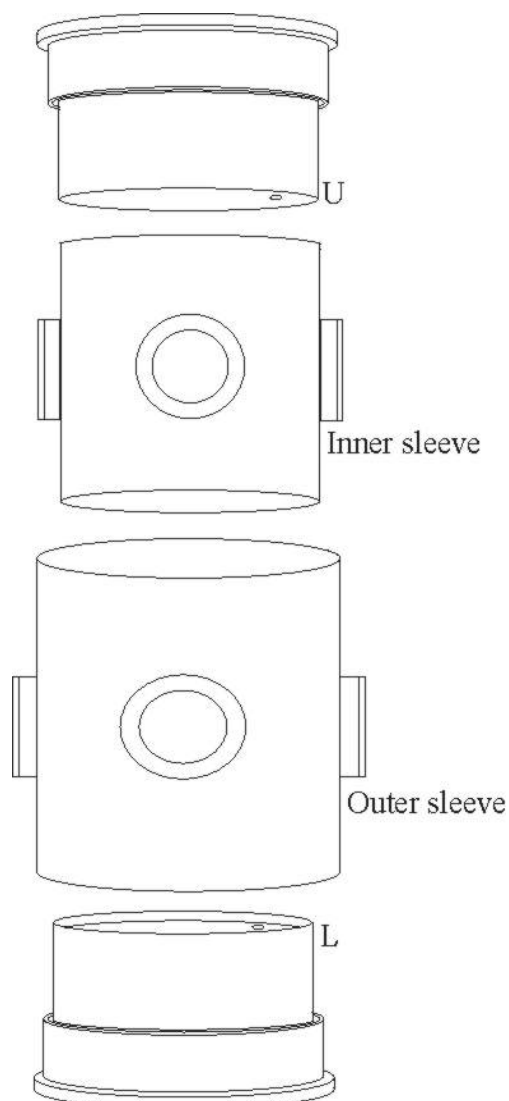


Figure 11: Diagram of the stainless steel cell separated into the four major components.

The inner sleeve fits snugly over the cylindrical upper and lower sections. The outer sleeve then fits over the inner sleeve and fits snugly over the bottom cylindrical piece of each of the other two sections. This was all screwed tightly together with large rods, not shown in this diagram, coming off the bottom section, to form a vacuum seal. The improved temperature regulation of this system is considered to be mainly the result of the large masses of stainless steel used in its construction, together with a slightly improved temperature-control algorithm, and the use of four small tube heaters inserted in each of the steel blocks in place of the two nichrome heating coils immersed in the coolant flows of the previous system.

2.2.1 Drying of sample

The *p*-tert-butyltoluene sample was dried using calcium hydride in the same manner as described for the initial metal cell, however the dried liquid sample was added directly to the cell. NMR spectroscopy was carried out on the sample to ascertain its purity, in an effort to rule out contamination as a reason for the erratic values from the original cell. The spectrum of the sample was found to have no detectable impurities when compared with a spectrum from The Aldrich library of ^{13}C and ^1H FT NMR spectra.

2.2.2 Degassing of sample

The cell used in this part of the experiment was easily detached from the vacuum system and was designed to be pulled apart into several sections, as can be seen in Figure 11. This meant the sample could be placed directly onto the bottom plate before the cell was reassembled and reattached to the vacuum system.

The cell was then cooled down to approximately $-20\text{ }^\circ\text{C}$, using a Haake DC5 circulating cryostat, and pumped on to remove dissolved gases. The temperature of $-20\text{ }^\circ\text{C}$ was not low enough to freeze the sample but was low enough to prevent a significant amount of liquid being pumped off when the cell was opened up to vacuum.

all in one block as might be suggested by the figure above. Monoethylene glycol (ordinary green antifreeze) was pumped through the compartments C_0 and C_1 from a Haake DC5 circulating cryostat. A and B indicate tubes leading to and from the cryostat. T_0 and T_1 represent two platinum resistance thermometers, as in Figure 10. The tube marked pressure was connected up to an MKS Baratron, type 627B, pressure transducer, which had a pressure range of 0 to 0.25 Torr. R indicates stainless steel rods, used to hold the apparatus tightly together. V indicates a tube connecting the vacuum jacket to the vacuum pump. The inner compartment consists of a stainless steel cylinder with the two plates, separated by a distance of 5mm, and four windows, W. This was separated from the atmosphere by the vacuum jacket, which also contained four windows, W.

The design of this cell was different from that of the previous cell due to the fact that it was intended for the measurement of CO_2 vapour over water. It has eight windows in total, four of which are made of fused silica and four are made of barium fluoride. The four barium fluoride windows enable the measurement of gas partial-pressures with an infrared diode laser.

This cell regulated the temperatures of both plates to within ± 0.02 °C of the target temperature, which was within the limits required for this experiment.

2.2.4 Measurement procedure

The measurement procedure using this cell was much the same as that for the previous cell. A similar QuickBasic program was used to record plots of both the temperatures and pressure and for temperature regulation. Measurements were again taken starting from high ΔT values towards $\Delta T = 0$ followed by measurements starting at $\Delta T = 0$ working back to high ΔT values. The measurements of Q^* at each temperature again had to agree at least three times before the reverse run was conducted. However, this time the temperatures were maintained to within ± 0.02 °C of the target value, which gave much more consistent results. The entire procedure was completed for four different temperatures of the lower plate: 5, 0, -10 and -20 °C.

2.2.5 Analysis of raw data

The data was again manipulated using Equation 30 to obtain values for Q^* using a plot of P versus ΔT . Errors for Q^* values were calculated using 95 % confidence limits for the initial slopes of plots such as that in Figure 3(b). The data was then analysed using a Basic program written by Professor Phillips, which calculated several variables associated with temperature jumps. The variables calculated were the temperature jump coefficients, ζ , and the thermal accommodation coefficients, α , associated with the temperature jumps. The values of α were then used to estimate the adsorption, θ , which is the fractional surface coverage [41]. A value for θ was found using the following equation:

$$\theta = \frac{\alpha - \alpha_{dry}}{\alpha_{wet} - \alpha_{dry}} \quad (32)$$

where α_{dry} is the accommodation coefficient when the upper plate is dry and α_{wet} is the accommodation coefficient when the upper plate is wet. Plots of θ against P/P_0 , where P_0 is the vapour pressure at the top plate, were used to determine the type of adsorption isotherm that best represents the systems investigated.

2.3 Water with N₂O vapour above

2.3.1 Degassing of sample

The metal cell of Figure 12 was used for this experiment; however, the degassing chamber was also used in this case. The degassing chamber can be seen in Figure 13. The water was sent into the cold finger through a funnel, shown as F, through into the chamber and then isolated by a stopcock. With the stopcocks to and from the chamber all closed off the water then underwent a series of freeze-pump-thaw-boil cycles, much like the procedure for *p*-tert-butyltoluene. It was frozen by filling the hollow inner cylinder with liquid nitrogen, then the sample was opened to the vacuum system for a time, then closed off again, thawed with the hot-air gun, and heated to boiling. Once the water was thoroughly degassed it was sent across into a glass bulb, which was attached to a bellows,

indicated by the symbol B. This allowed for the liquid to be manually sent into the cell by adjusting the bulb to sit at the same level as the lower plate in the cell until water could be seen covering the bottom plate. The V in Figure 13 indicates the vacuum system.

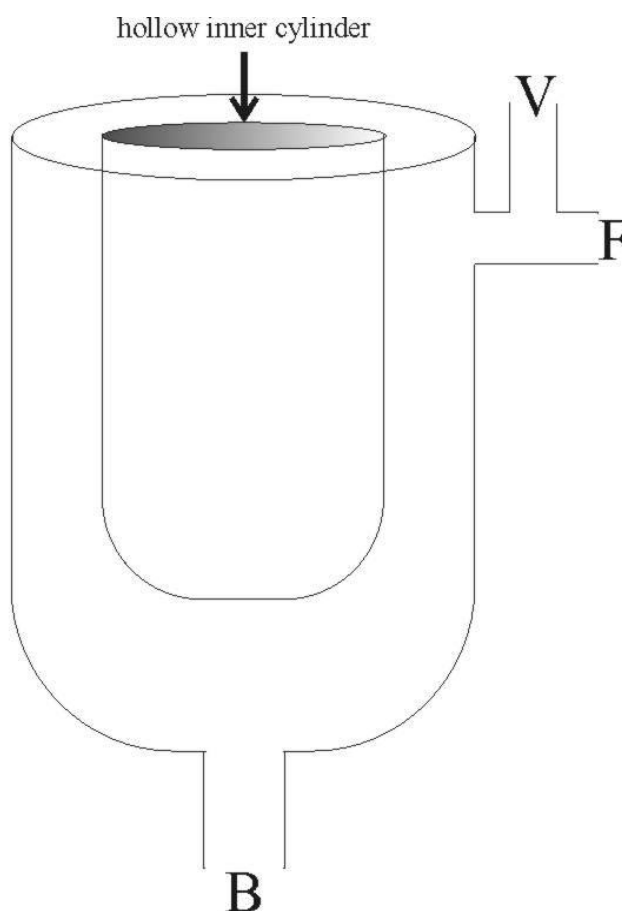


Figure 13: Degassing chamber.

2.3.2 Introduction of N_2O into the cell

Once the water was in the cell N_2O was admitted from a bulb attached to the vacuum system. The vacuum pump was closed off and the valve to the cell was opened. The stopcock to the N_2O bulb was opened slowly to release the gas into the system until a particular pressure could be seen on the Baratron attached to the cell. The cell was then left overnight to allow the gas to come to equilibrium with the water.

2.3.3 Diode laser setup

The procedure required for pressure measurements when an additional gas, in this case N_2O , is put in the cell is slightly more complex than for the previous experiments. Infrared laser detection was used in order to obtain spectra over the various temperatures to ascertain partial-pressure values. The apparatus involved had been set up by Professor C. J. Pursell and a diagram of the entire setup can be seen in Figure 14. (A more detailed schematic of the L5002 Optical Baseplate can be seen in Figure 15.)

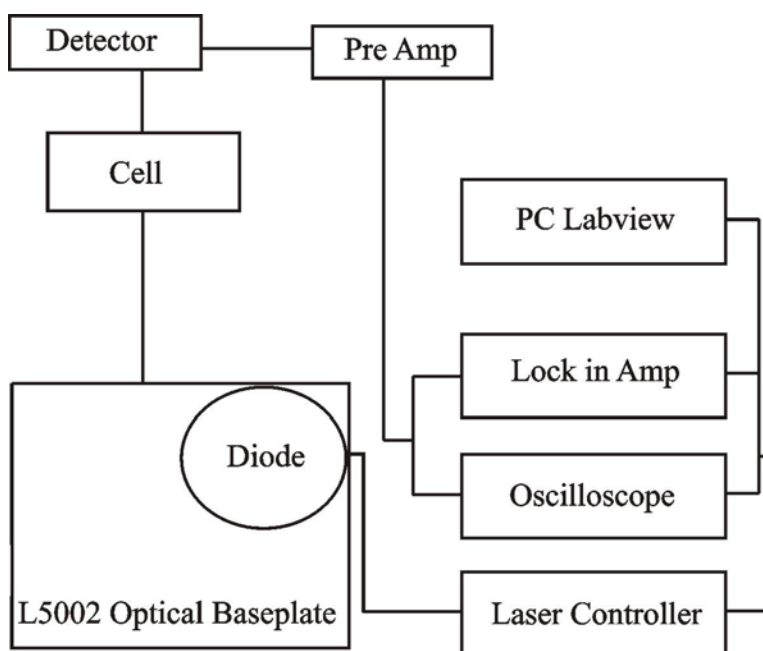


Figure 14: Schematic of the laser setup.

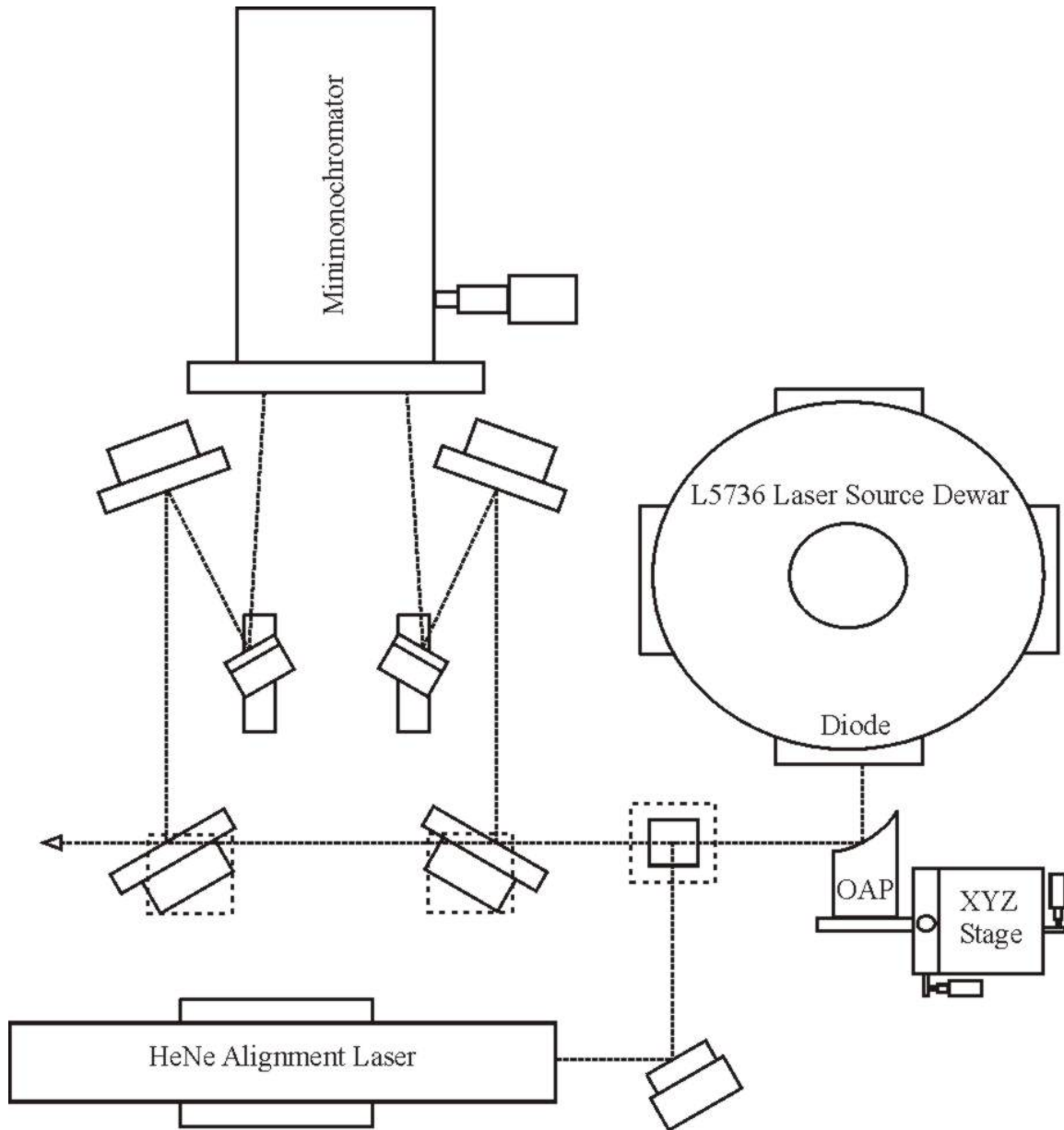


Figure 15: Schematic of the L5002 Optical Baseplate.

The diode was an L5700 series infrared tunable diode laser consisting of a small, single-crystal, lead-salt chip mounted in a gold-plated copper package. The laser was installed in an L5736 Laser source Dewar, which was a liquid nitrogen Dewar designed to provide cryogenic cooling for operation of the tunable diode laser. It allowed for the operation of the diode laser with a precisely defined current at a precise temperature in the 80 K to 120 K temperature range.

The Helium Neon (HeNe) Alignment Laser was used to roughly align the off-axis parabola, OAP, to the diode laser. The beam from the HeNe Alignment Laser was observed reflected off the OAP entering the Dewar window. The aim at this point was to adjust the horizontal (X) and vertical (Y) stages to bring the HeNe spot as closely as possible onto the active region of the diode laser chip. This was necessary because, when working with an infrared source, alignment becomes difficult as the beam cannot be seen, so the visible output of the HeNe laser is adjusted to be collinear with the infrared beam. The focus of the OAP (Z) was adjusted separately. The HeNe laser was coupled to the optical axis by means of a cube beamsplitter. The beamsplitter, indicated by the solid square enclosed in a dashed square, was removed when not using the HeNe Laser.

The laser itself was controlled using the Model L5830 Tunable Diode Laser (TDL) Controller. The TDL Controller was used to control the temperature and current of the laser. There is also a modulation control, which enables the selection of a particular output waveform by adjusting the modulation of the diode current.

In most of the experiments the IR beam was modulated using a Model 300C variable frequency rotary chopper, which was located to the left of the Optical Baseplate in line with the dashed line with the arrowhead. The signal was then detected with a liquid-nitrogen cooled InSb detector coupled to a matched preamplifier, the output of which was sent to a Princeton Applied Research HR-8 lock-in amplifier.

Alternatively, instead of using the rotary chopper, the diode output was modulated with a saw-tooth waveform, and the detected signal was sent to a Fluke Combiscope digital oscilloscope, from which the program FlukeView provided a snapshot of the infrared spectrum of interest over a range of about 1 cm^{-1} , which could be viewed on the computer screen or saved as a data file.

2.3.4 Measurement Procedure

A particular portion of the N₂O infrared vibration spectrum was chosen for N₂O, and measurements were taken starting at high ΔT values and working down to $\Delta T = 0$. The sample was left to equilibrate for 20 minutes after the initial temperature change of the upper plate. A spectrum was then acquired. The total pressure was also measured at this point. This was repeated twice for each ΔT value, that is, every 20 minutes for an hour before moving on to the next ΔT value. Taking three measurements at every ΔT value allowed the observation of any changes in the spectrum over time due to a greater or lesser amount of N₂O dissolving in the water. The results obtained were found to be scattered over time and it was realised that a new diode with a different modal range was required for this experiment. The existing laser diode had many modes of oscillation, with mode gaps between them, and a tendency to operate in several modes at once. A degree of mode selection was possible with the mini-monochromator that was part of the system, but the output was still not sufficiently pure to allow precise concentration measurements with the necessary level of precision. Hence this part of the project was suspended pending the arrival of a new single-mode diode.

Chapter 3: Results and Discussion

3.1 Analysis of data in terms of the Onsager heat of transport

The initial data, obtained using the cell shown in Figure 10, were scattered and inconsistent. A number of experiments were completed with the base temperature held at 0 °C, starting at ΔT equal to zero and increasing to larger ΔT values, but the results were still inconsistent. Several experiments were also carried out starting at large ΔT values and working down to zero; these also proved unreliable. Other base temperatures gave similarly scattered data. Extensive leak testing was carried out on the cell and surrounding apparatus to ensure this was not the cause of the erratic results. However, the inconsistency of the results was subsequently thought to be due to the lack of sensitivity in the temperature regulating system. The cell shown in Figures 11 and 12 was then used instead with more success, as mentioned in Section 2.2.

Plots of pressure against temperature difference were found to be similar in shape to those previously obtained for aniline, *n*-heptanol and water. There was an initial linear slope with an abrupt change at approximately $\Delta T = 1$ followed by a section with a more gradual slope (Figure 16). These results support the idea of temperature jumps as the reason for the abrupt change in gradient, as mentioned in Section 1.3, and analysis of the data with respect to these temperature jumps will be carried out in Section 3.2.

However, this particular shape only holds for the results taken starting at low ΔT values. The results obtained working from large ΔT values down towards $\Delta T = 0$ were unlike those obtained previously. A noticeable discrepancy with these results is the value of the pressures at $\Delta T = 0$. The equilibrium pressure for these results was generally too high by at least 0.01 Torr; the results were also less reproducible, especially at large ΔT values. However, two trends emerged. A linear portion with a positive gradient was generally observed at low ΔT values and P tended to decrease as ΔT increased at larger values of ΔT , as can be seen in Figure 17. The shape of these plots can probably be rationalised in terms of very large temperature jumps at the top plate, but more work is required in order to establish what is going on. So, although results

have been obtained working from large ΔT values downwards, only those working from $\Delta T = 0$ upwards were used for analysis in terms of Q^* .

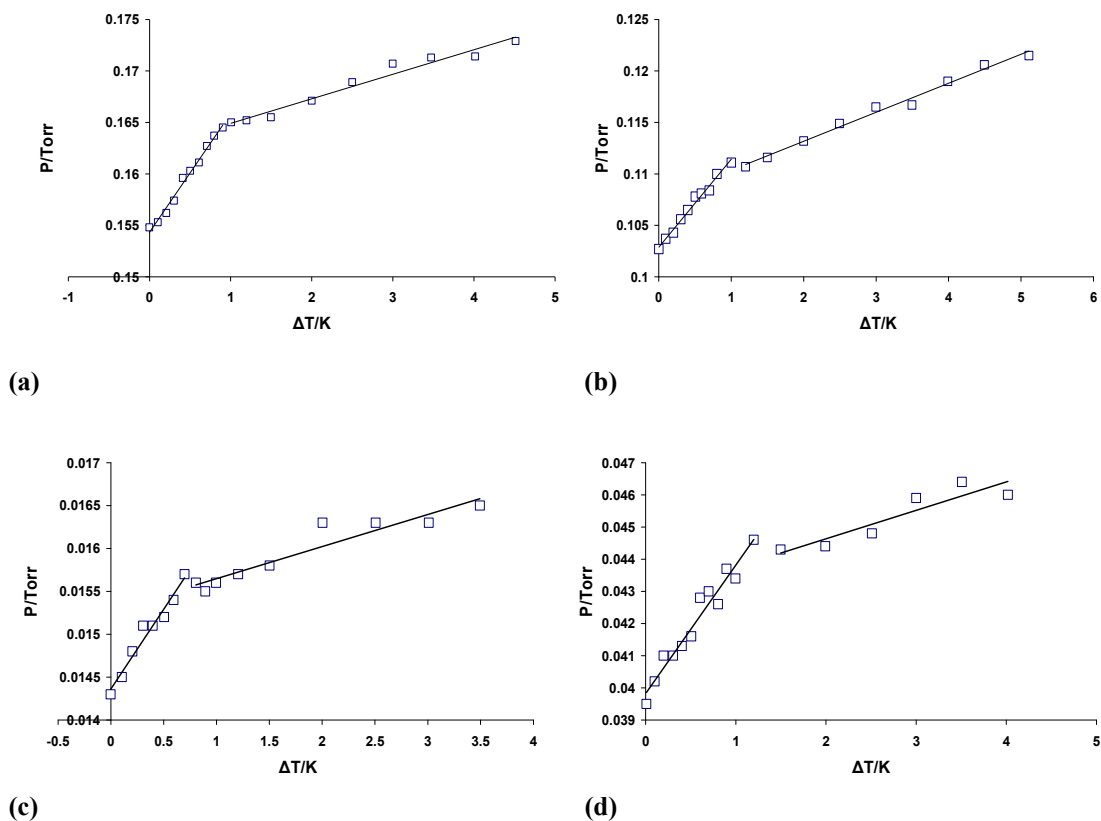


Figure 16: Representative plots of P as a function of ΔT for p -tert-butyltoluene when working from low ΔT values up to large ΔT values. The liquid surface temperatures are (a) $5^\circ C$, (b) $0^\circ C$, (c) $-20^\circ C$ and (d) $-10^\circ C$.

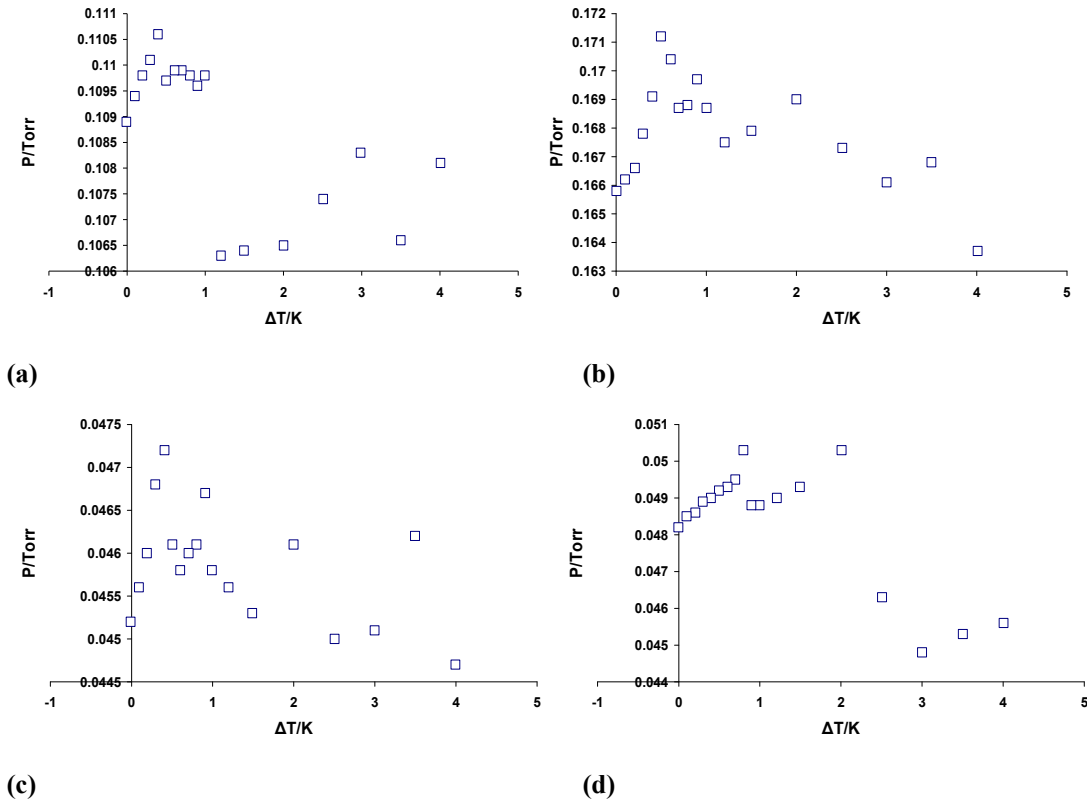


Figure 17: Plots of P as a function of ΔT for *p*-tert-butyltoluene when working from large ΔT values down to ΔT equals zero. The liquid surface temperatures are (a) 0 °C, (b) 5 °C, (c) -10 °C and (d) -10 °C.

The important section of these plots in terms of the Onsager heat of transport (Q^*) is the initial linear slope at low ΔT values, as explained in detail in Section 1.3. Q^* values were calculated using Equation 30, from the gradient of plots of pressure against the applied temperature difference, ΔT , as seen in Figure 16. Equation 30 is rearranged to obtain Q^* , giving the following equation:

$$Q^* = -\left(\frac{\Delta P}{P} \frac{T}{\Delta T}\right)RT = -\left(\frac{\Delta P}{\Delta T}\right) \frac{RT^2}{P} \quad (33)$$

Where $(\Delta P/\Delta T)$ is the initial slope of the plot, R is the ideal gas constant, T represents the temperature of the bottom plate and P is the pressure when ΔT equals zero, i.e. the value of the y-intercept on the plot. The Q^* values obtained are summarised in Table 1 along with their corresponding uncertainty, which was calculated as a 95 % confidence limit for the initial slopes, using Student's *t*.

Table 1: $|Q^*|$ results for *p*-tert-butyltoluene calculated from the initial slope of a plot of P against ΔT :

Temperature (°C)	Number of mean free paths (n_λ)	$ Q^* $ (kJ mol ⁻¹)
-20	6.0	69.0 ± 4.6
-20	6.0	74.9 ± 11.2
-20	6.0	49.7 ± 15
-10	12.5	56.6 ± 10.3
-10	12.5	59 ± 12.5
-10	12.5	51.5 ± 14
0	26.3	55 ± 11.4
0	26.3	52.1 ± 5.2
0	26.3	52.6 ± 11.1
5	38.1	51.6 ± 14
5	38.1	46.7 ± 4.3
5	38.1	43.4 ± 11.7
5	38.1	47.7 ± 8.3

The Q^* values (calculated as a weighted mean value for each temperature) for the $T = -20, -10, 0$ and 5 °C systems were 65 ± 11 kJ mol⁻¹, 56 ± 12 kJ mol⁻¹, 53 ± 10 kJ mol⁻¹ and 47 ± 12 kJ mol⁻¹, respectively. With the exception of the first two values, at a base temperature of -20 °C, the Q^* values are all within a range of -43 to -59 kJ mol⁻¹. The average $|Q^*|$ value (including the top two values in Table 1, at $T = -20$ °C) is 55 ± 11 kJ mol⁻¹ (calculated as the weighted root mean square of the 95 % confidence limits). This is equal, within the specified uncertainty, to the latent heat of vaporisation (ΔH_{vap}) for *p*-tert-butyltoluene, which is 51.8 kJ mol⁻¹. This result differs from previous experiments of this type, since with all previous results the Q^* values were generally about half the latent heat of vaporisation when outside the Knudsen zone. However, here Q^* is approximately the same magnitude as ΔH_{vap} even when n_λ is much greater than two, as can be seen in Figure 18.

Calculation of n_λ involves firstly calculation of the mean free path, λ , via the following equation:

$$\lambda = \frac{\bar{c}}{z} \quad (34)$$

where \bar{c} symbolizes the mean speed of the molecule and z represents the collision frequency. The expression for z is given by

$$z = \left(\frac{\sqrt{2}\sigma\bar{c}p}{kT} \right) \quad (35)$$

Where σ represents the collision cross section, p represents the equilibrium vapour pressure at T , k represents Boltzmann's constant and T represents the temperature. The collision cross section was estimated to be 1.0 nm^2 , by taking the value for benzene (similar in size to toluene), 0.88 nm^2 , and accounting for the larger size of *p*-tert-butyltoluene. Substitution of Equation 35 for z gives the following expression for λ

$$\lambda = \left(\frac{kT}{\sqrt{2}\sigma p} \right) \quad (36)$$

The mean free path is then converted to the number of mean free paths in the 5 mm vapour gap. That is,

$$n_\lambda = \frac{5}{\lambda} \quad (37)$$

Therefore n_λ was calculated for the various base temperatures and these were plotted against the $|Q^*|$ values to plot Figure 18.

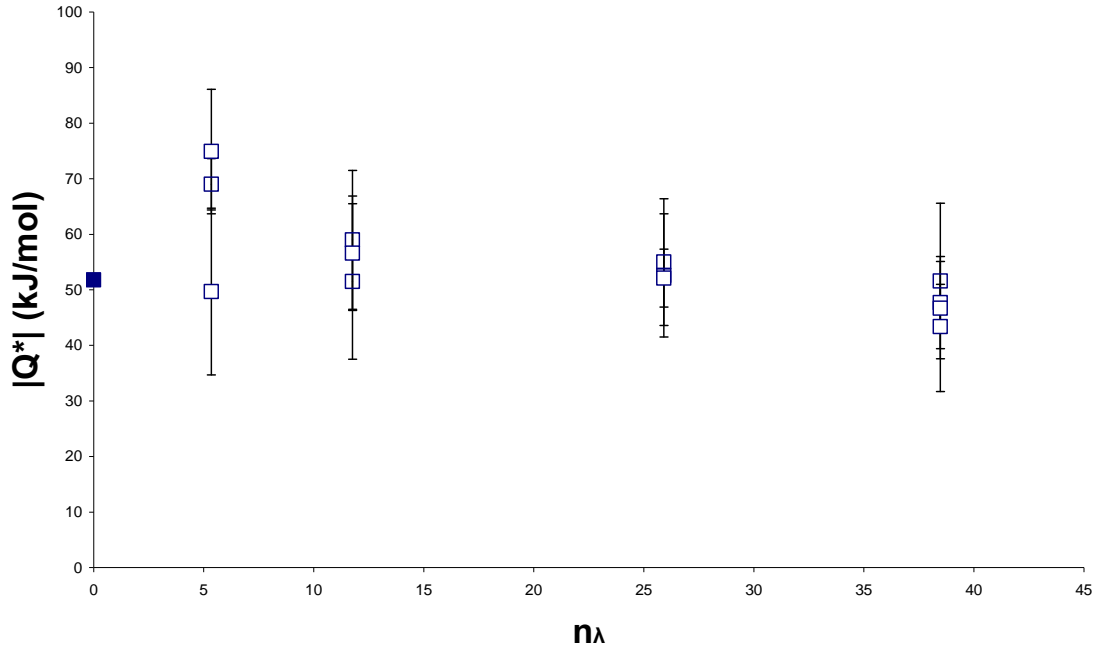


Figure 18: $|Q^*|$ values, for *p*-tert-butyltoluene, plotted as a function of the number of mean free paths, $n\lambda$, in the 5mm gap. The filled square indicates the value of ΔH_{vap} .

Figure 18 shows a relatively constant value for Q^* for the various base temperatures, a similar result to those found previously for aniline, *n*-heptanol and water when dealing with Q^* outside the Knudsen zone. A major difference is the remarkably large size of $|Q^*|$, which implies that there is always likely to be a significant amount of cool-to-warm distillation occurring with *p*-tert-butyltoluene. However, the plots in Figure 16 imply that cool-to-warm distillation ceases when ΔT is about 1 °C. The various problems posed by these results might be resolved by assuming that nucleation of *p*-tert-butyltoluene upon dry stainless steel is a very slow process, so that the results in Figure 17 do not correspond to a genuine stationary state in terms of Onsager's theory. In addition, the liquid film required to avoid a temperature jump is not strongly held on the surface of the upper plate, so that the data of Figure 16 come to resemble the water data as obtained by adjusting the upper-plate temperature.

A possible explanation for the large size of Q^* is that *p*-tert-butyltoluene is not an ideal gas and therefore R (Equation 33) must be replaced with $R(1+B/V)$, where B is the second virial coefficient, and is a function of temperature alone, and V is the volume per mole of

gas under the conditions of the experiment. Including this factor would probably lower the values of Q^* as calculated. However, it is apparent from comparison of the magnitude of the Q^* with the size of ΔH_{vap} that this correction is particularly important for *p*-tert-butyltoluene at -20 °C. For toluene, which is the closest compound to *p*-tert-butyltoluene for which values for B are available, the virial coefficients are large and negative. Some values for toluene found in the CRC Handbook of Chemistry and Physics and in a paper by J. D. Cox and R. J. L. Andon are presented in Table 2 [42, 43]:

Table 2: Virial coefficients for toluene at various temperatures.

Temperature (K)	Value of B ($\text{cm}^3 \text{mol}^{-1}$) (Handbook of Physics and Chemistry)	Temperature (K)	Mean value of B ($\text{cm}^3 \text{mol}^{-1}$) (Cox and Anton)
350	-1641	408.8	-1013
370	-1394	424	-940
390	-1195	437.6	-864

Table 2 shows that the virial coefficient increases in magnitude as the temperature decreases and hence would have the greatest effect on the Q^* values calculated for the lower temperatures. Recalculation of the latent heat of vaporisation for toluene, by Cox and Andon, showed insignificant changes in the value at 25 °C. The value we used for ΔH_{vap} derived from listed vapour pressures at temperatures above 0 °C. Hence, the larger virial coefficient at -20 °C might have made a significant difference to the present results.

3.2 Temperature jump analysis

The data obtained from the *p*-tert-butyltoluene experiments were analysed in the same way as the data from the experiments for water. The analysis involves calculating first the temperature jumps, then the jump coefficients, and finally the thermal accommodation coefficients for the vapour at the surface of the stainless steel upper plate. This procedure is only relevant for the results obtained where the upper plate was dry, i.e. slope₁, as depicted in Figure 6, of the *P* versus ΔT plots, as these plots are the only ones where temperature jumps have occurred.

The temperature jumps were calculated as detailed in Section 1.3, while the temperature jump coefficients were calculated using Equation 31 and the thermal accommodation coefficients (α) were obtained from the jump coefficients using the algorithm of Loyalka, Siewert and Thomas [44].

A Basic program, written by Professor Phillips, was used to calculate values for the temperature jumps, the temperature jump coefficients and the thermal accommodation coefficients. The thermal accommodation coefficients were plotted against the temperature of the upper plate to show the dependence of α on the temperature. The results for *p*-tert-butyltoluene were similar to those found for water (Figure 19) and are presented in Figure 20.

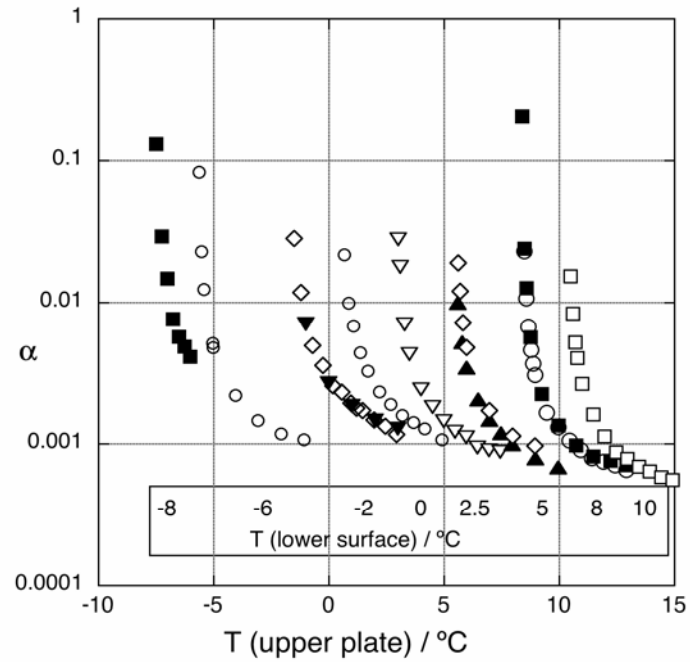


Figure 19: Thermal accommodation coefficients for water, on stainless steel, from a set of experimental runs over the temperature range -8 to 10 °C [30].

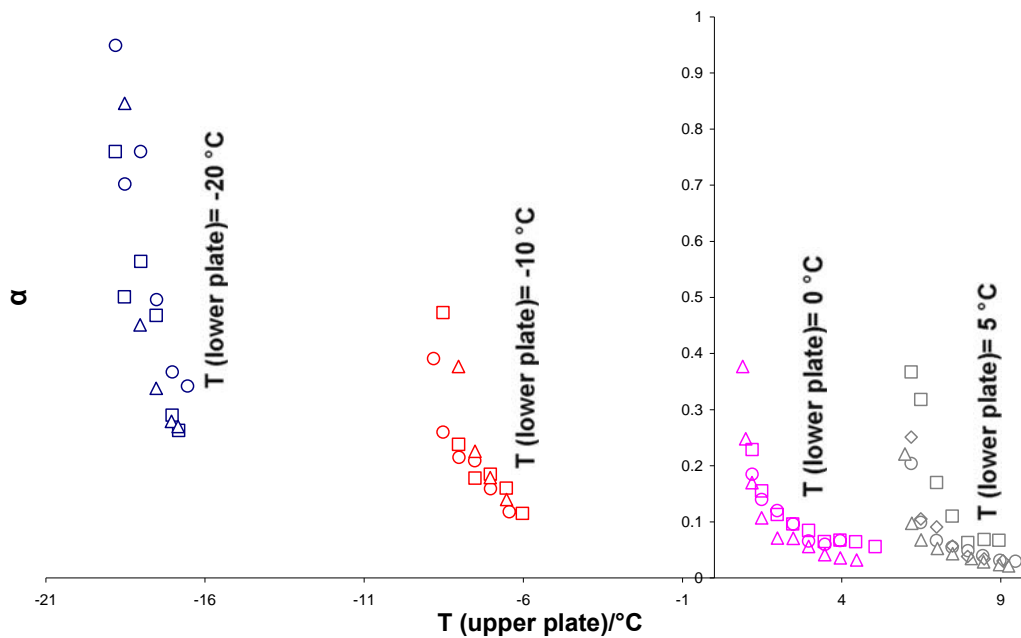


Figure 20: Thermal accommodation coefficients for *p*-tert-butyltoluene on stainless steel, for all experiments over the temperature range -20 to 5 °C.

F

Figures 19 and 20 show the dependence of α on the temperature of the upper plate. The overall similarity of these curves supports the view that the temperature difference between the liquid surface and the upper plate plays the major role in determining the value of α , as it can be clearly seen that α alters with respect to ΔT alone [30]. This provides a potentially important new method of measuring thermal accommodation coefficients for a variety of surfaces and vapours.

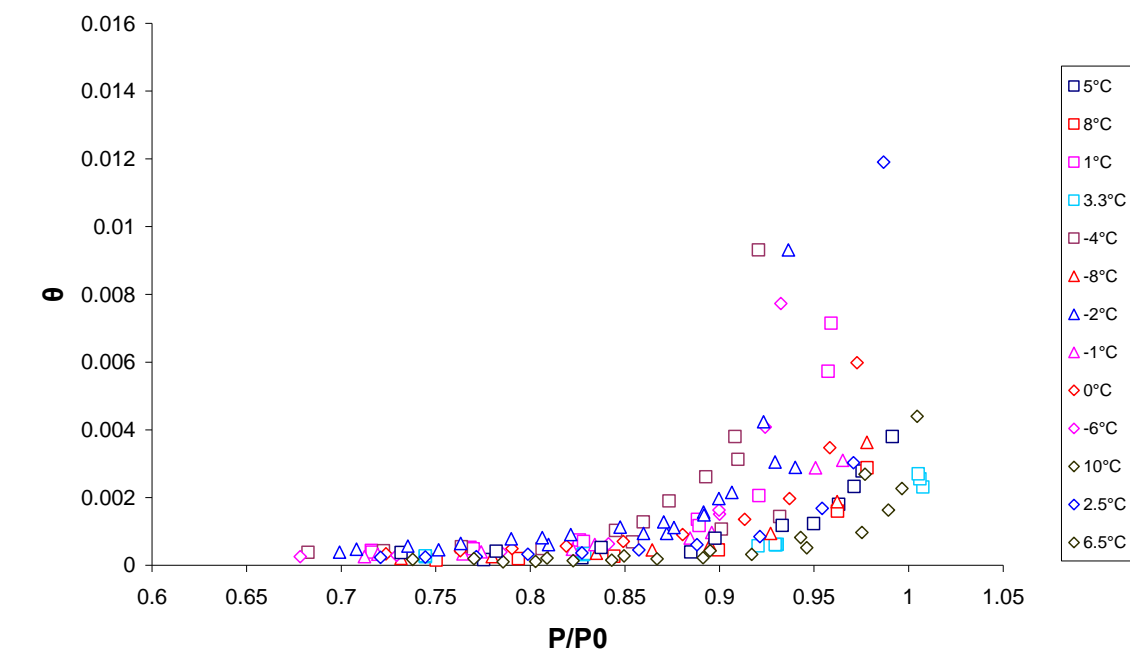
3.3 Adsorption isotherm analysis

The data obtained from the experiments with *p*-tert-butyltoluene were also analysed in terms of adsorption isotherms, as were the data obtained by Professor Christopher Pursell for water. Values for θ , the fractional coverage of the surface, were calculated for all the data using the calculated values for α , from temperature jump analysis, and substituting them into Equation 32, shown below:

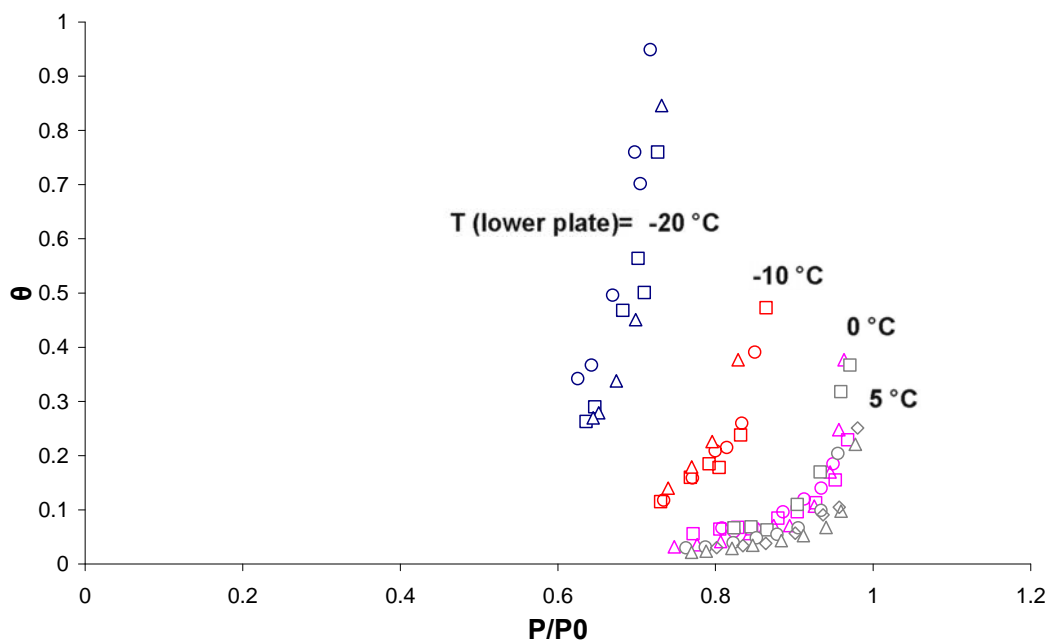
$$\theta = \frac{\alpha - \alpha_{dry}}{\alpha_{wet} - \alpha_{dry}} \quad (32)$$

Equation 32 is a hypothesis based on a model in which a partially covered metal surface has discrete wet and dry zones. The value for α_{wet} was assumed to be unity, since here the water molecules are striking a wet surface, and α_{dry} was assumed to be approximately 1×10^{-4} .

θ was then plotted against $\frac{P}{P^0}$, where P^0 is the vapour pressure at the upper plate, to determine the type of adsorption isotherm that best represents the systems investigated, as can be seen in Figure 21, for both water (a) and *p*-tert-butyltoluene (b).



(a)



(b)

Figure 21: Fractional adsorption for (a) water on stainless steel, for experiments over the temperature range -8 to 10°C and (b) *p*-tert-butyltoluene on stainless steel, for experiments over the temperature range -20 to 5°C .

The form of these plots implies that the results should be fitted to a BET isotherm. The BET isotherm is the most commonly used isotherm, dealing with multilayer adsorption. The original equation for this isotherm, as derived by Brunauer, Emmett and Teller, is:

$$\frac{n}{n_{mon}} = \frac{cz}{(1-z)\{1-(1-c)z\}} \quad (38)$$

where n represents the moles of gas adsorbed at the equilibrium pressure P ; n_{mon} is the number of moles of gas adsorbed when the surface is completely covered by a monomolecular layer; z represents the relative pressure (P/P^*), P^* being the vapour pressure of the liquid adsorbate; and c is a constant, which depends on the relative strengths of adsorption to the surface and condensation of the pure adsorbate [41, 45, 46].

Brunauer et al. also proposed a linear transformation of Equation 38 into:

$$\frac{z}{n(1-z)} = \frac{1}{n_m c} + \frac{c-1}{n_m c} z \quad (39)$$

The linearity of this BET representation is reduced to a particularly narrow range ($z = 0.05-0.35$) and it has been observed that for some systems this range is reduced further still [45-47]. More recent work by Sánchez-Montero et al. includes a review of the BET plot proposing three additional linear transformations of the original equation, Equation 38, which can be used to investigate the BET model. The other possible linear forms are:

$$\frac{z}{n(1-z)^2} = \frac{1}{n_m c} + \frac{1}{n_m} \frac{z}{1-z} \quad (40)$$

$$\frac{n(1-z)^2}{z} = n_m c - cn(1-z) \quad (41)$$

$$\frac{1}{n(1-z)} = \frac{1}{n_m} + \frac{1}{n_m c} \frac{1-z}{z} \quad (42)$$

Some of these equations have clear advantages to the original BET transformation. For example, by using Equation 40 n_m can be obtained directly from the slope of the line.

However, n/n_m was replaced with θ ($\theta = n/n_m$) and the equations were rearranged accordingly to give the Equations 43, 44, 45 and 46 respectively:

$$\frac{z}{\theta(1-z)} = \frac{1}{c} + \frac{c-1}{c} z \quad (43)$$

$$\frac{z}{\theta(1-z)^2} = \frac{1}{c} + \frac{z}{1-z} \quad (44)$$

$$\frac{\theta(1-z)^2}{z} = c - c\theta(1-z) \quad (45)$$

$$\frac{1}{\theta(1-z)} = 1 + \frac{1}{c} \frac{1-z}{z} \quad (46)$$

In general a linear relationship was observed only with Equation 44. However, several data sets also produced a near linear relationship for the original transformation, Equation 43.

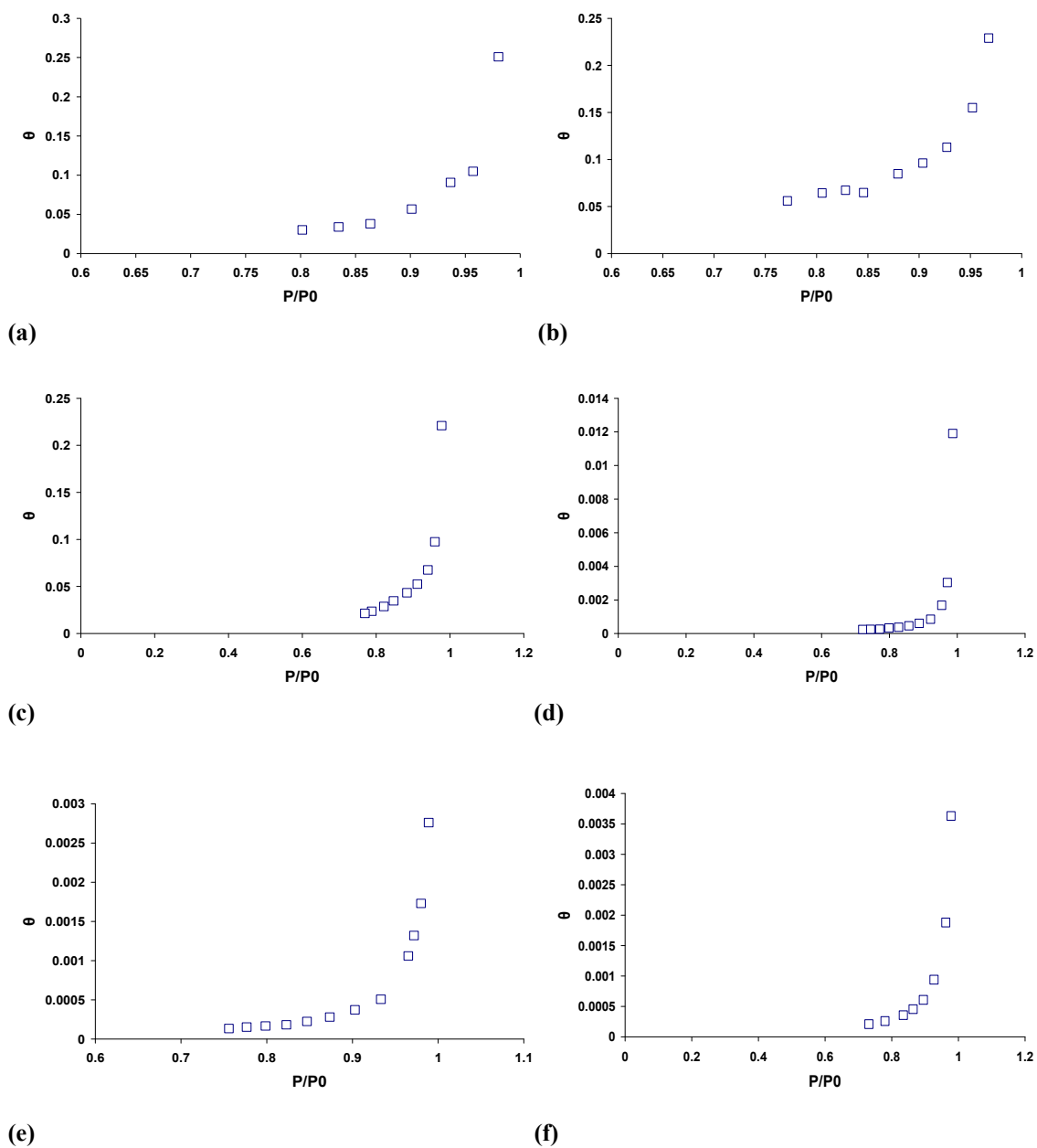


Figure 22: Typical isotherms for (a) p -tert-butyltoluene, (b) p -tert-butyltoluene, (c) p -tert-butyltoluene, (d) water, (e) water and (f) water. The lower surface temperatures are 5, 0, 5, 2.5, 8 and -8 °C respectively.

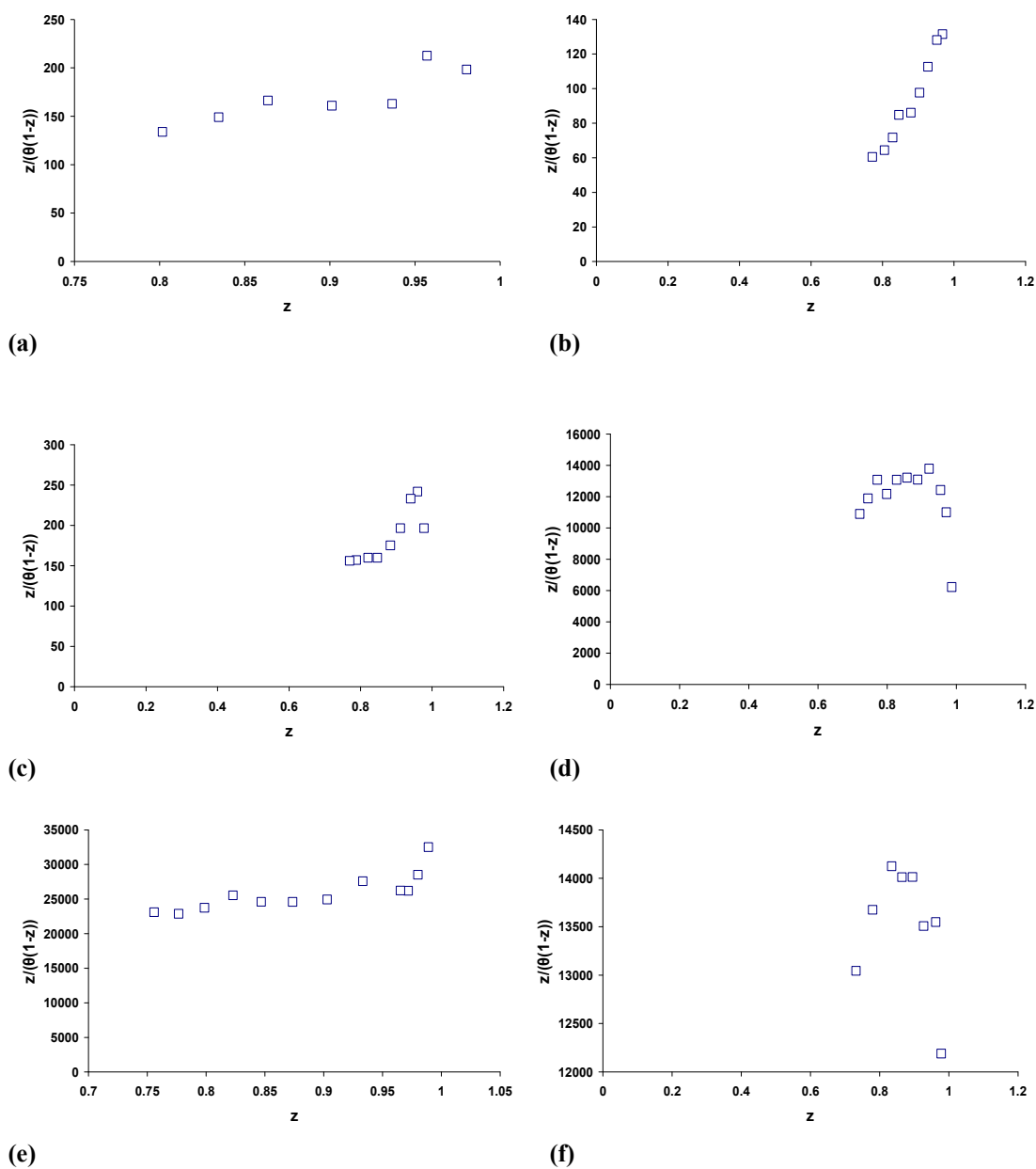


Figure 23: Typical plot using the original BET linearisation derived by Brunauer et al. for (a) p -tert-butyltoluene, (b) p -tert-butyltoluene, (c) p -tert-butyltoluene, (d) water, (e) water and (f) water. The lower surface temperatures are 5, 0, 5, 2.5, 8 and -8 °C respectively.

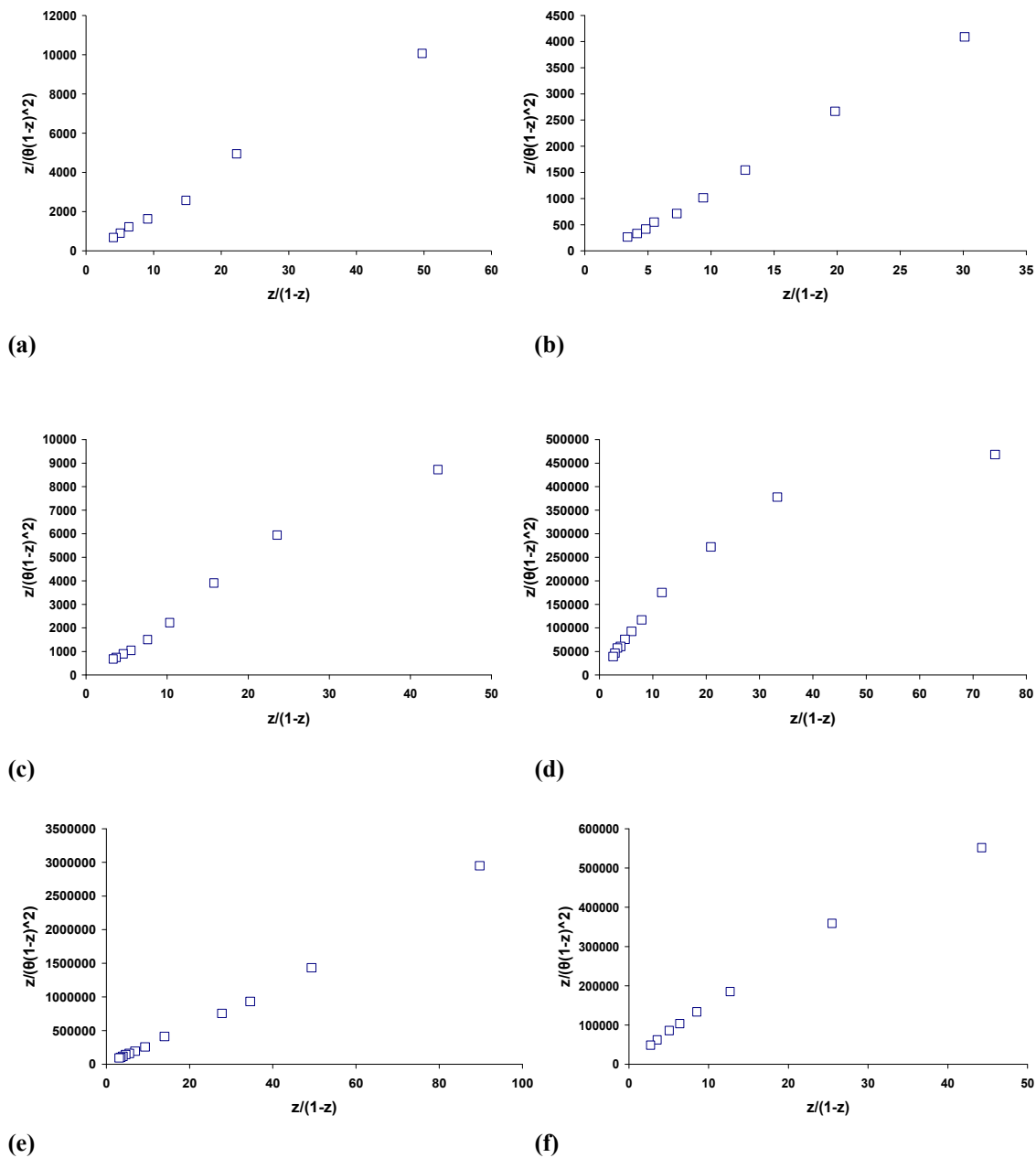


Figure 24: Typical plot using equation (44) for (a) p -tert-butyltoluene, (b) p -tert-butyltoluene, (c) p -tert-butyltoluene, (d) water, (e) water and (f) water. The lower surface temperatures are 5, 0, 5, 2.5, 8 and -8 °C respectively.

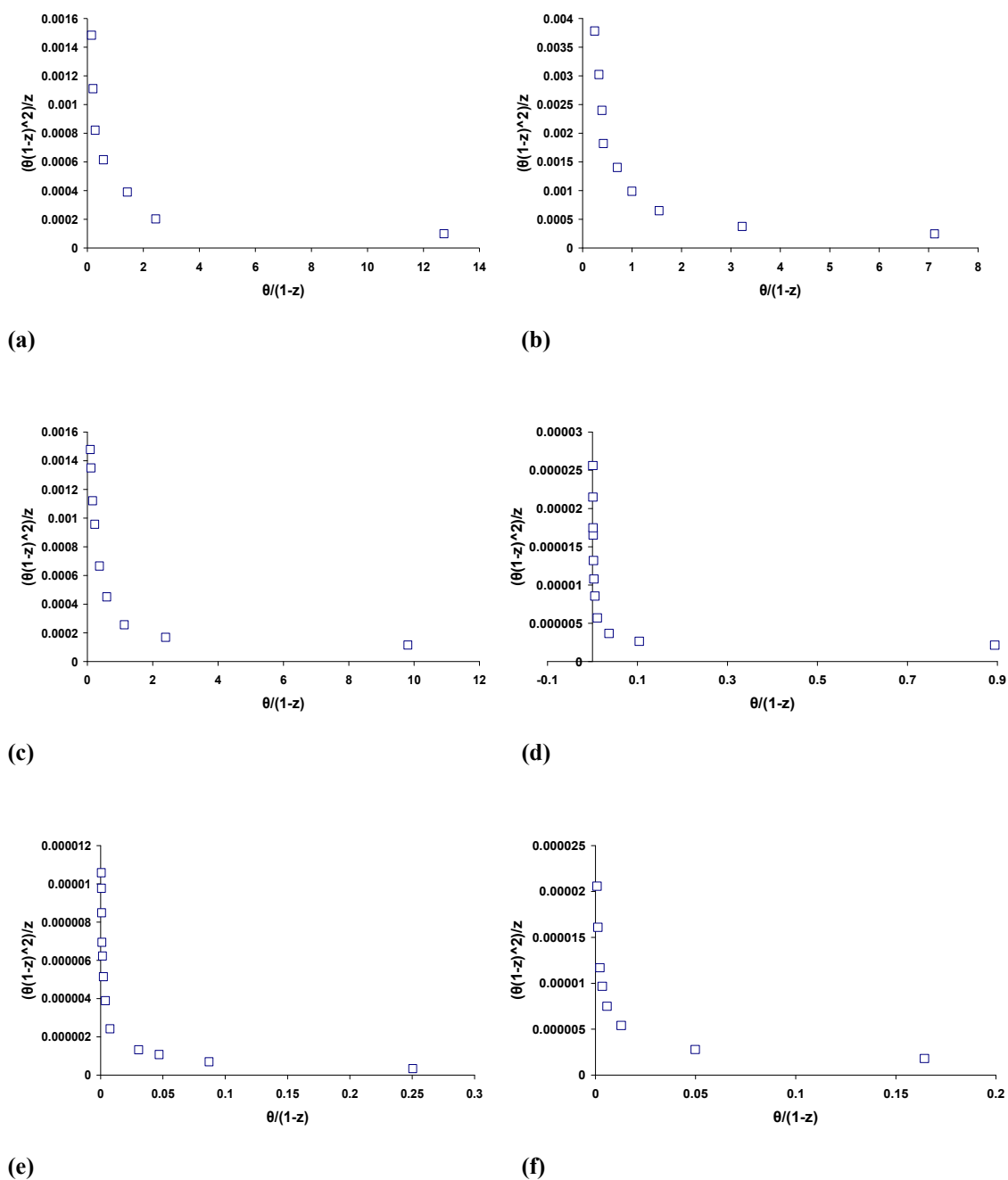


Figure 25: Typical plot using equation (45) for (a) p -tert-butyltoluene, (b) p -tert-butyltoluene, (c) p -tert-butyltoluene, (d) water, (e) water and (f) water. The lower surface temperatures are 5, 0, 5, 2.5, 8 and -8 °C respectively.

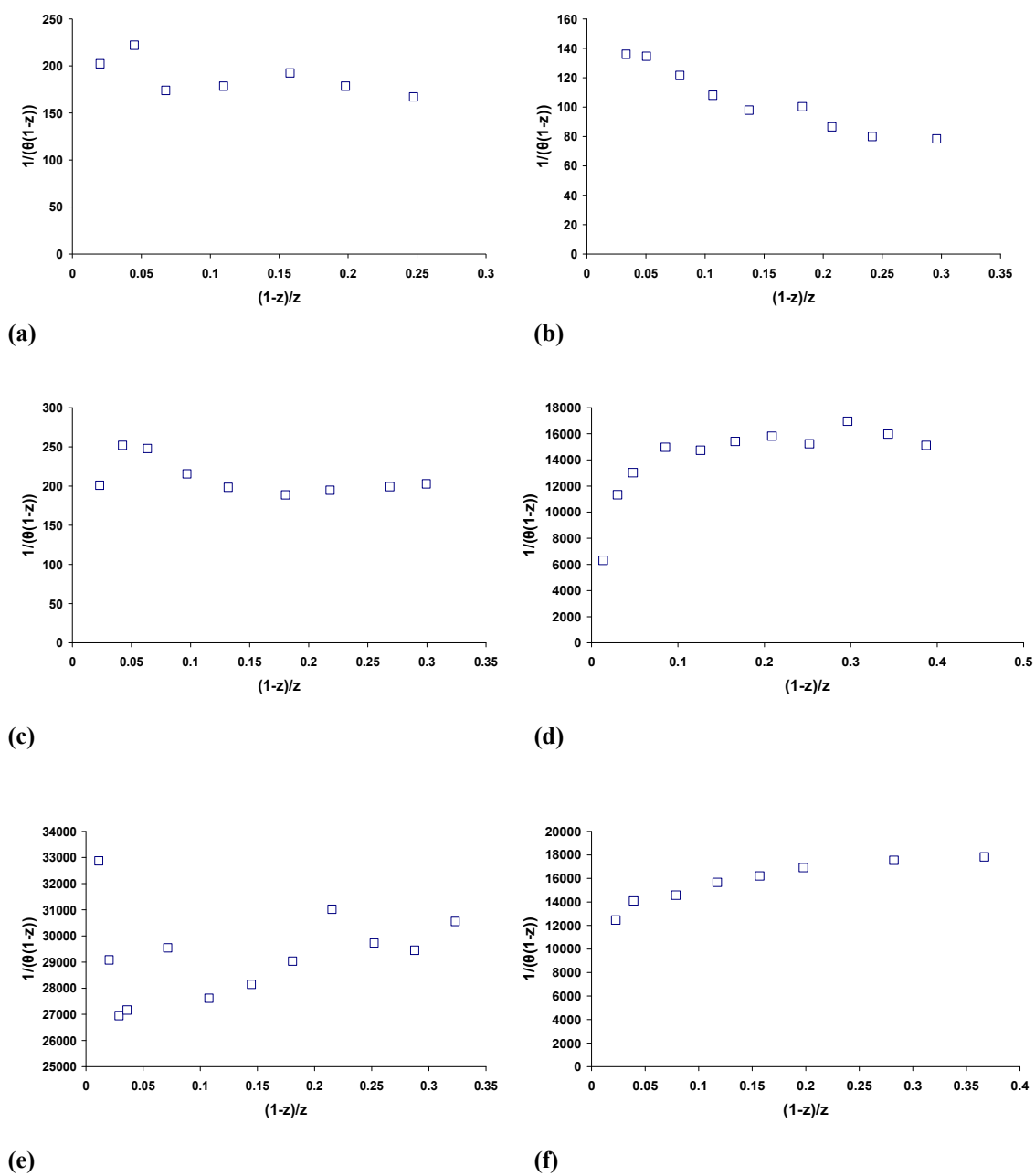


Figure 26: Typical plot using equation (46) for (a) p -tert-butyltoluene, (b) p -tert-butyltoluene, (c) p -tert-butyltoluene, (d) water, (e) water and (f) water. The lower surface temperatures are 5, 0, 5, 2.5, 8 and -8 °C respectively.

Figures 23 to 26 show the general relationships observed when the four different linearisations, Equations 43 to 46, were applied. The non-linearity observed for Equations 45 and 46 (Figures 25 and 26) is attributed to the non-constant value of the c parameter, as found in previous experiments by Sánchez-Montero et al. They obtained similar linear results from analyses with Equations 43 and 44. They also demonstrated that the c parameter is not a constant and instead varies along the isotherm [45]. This can be shown by plotting the c parameter, as calculated by Equation 47, against the amount of surface coverage (Figure 27).

$$c = \frac{\theta(1 - z)^2}{z[1 - \theta(1 - z)]} \quad (47)$$

(Equation 47 is obtained from the original BET model.) These figures demonstrate that the c parameter is not a constant and varies, and in fact decreases, with increased surface coverage.

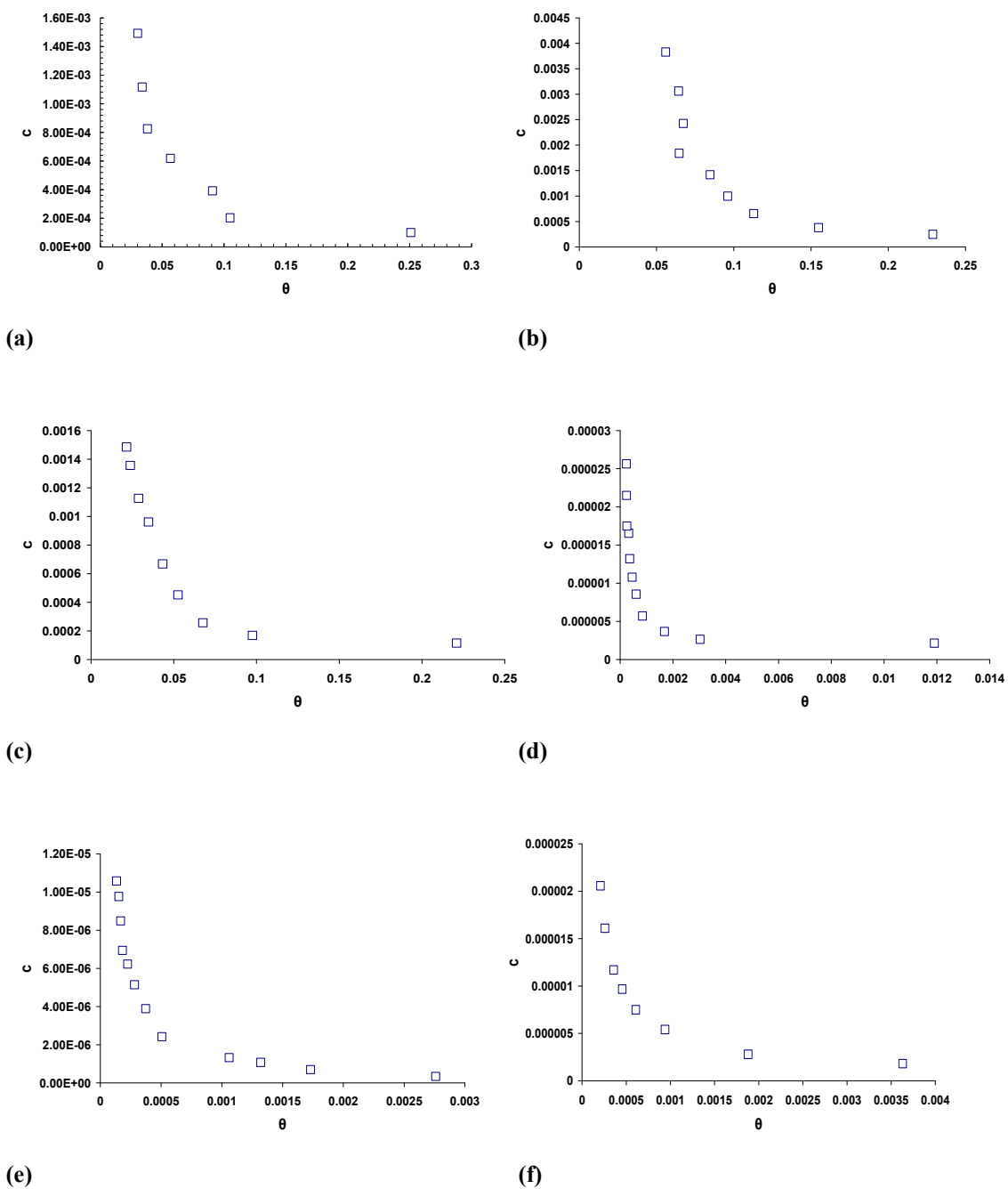


Figure 27: Typical plot of the variation in the c parameter against surface coverage for (a) p -tert-butyltoluene, (b) p -tert-butyltoluene, (c) p -tert-butyltoluene, (d) water, (e) water and (f) water. The lower surface temperatures are 5, 0, 5, 2.5, 8 and -8 °C respectively.

The results obtained by Sánchez-Montero et al. led them to the conclusion that the linearity obtained when using Equations 43 and 44 would only be seen if the c parameter

took on high values and that if c were to have small values the linearity would cease to exist. Hence they concluded that the c parameter controls the range over which the BET representation is linear [45]. This theory also explains why the Type III and V (see Figure 28 for the five general types of isotherm for physical adsorption) isotherms do not fit the BET model, as these isotherms are obtained with low c values [45]. This may also account for the fact that the plots using Equation 43 for both *p*-tert-butyltoluene and water do not show a particularly linear relationship, as the c parameter takes on small values in these two cases. The isotherms obtained for water and *p*-tert-butyltoluene do indeed appear to have the shape of the Type III isotherms.

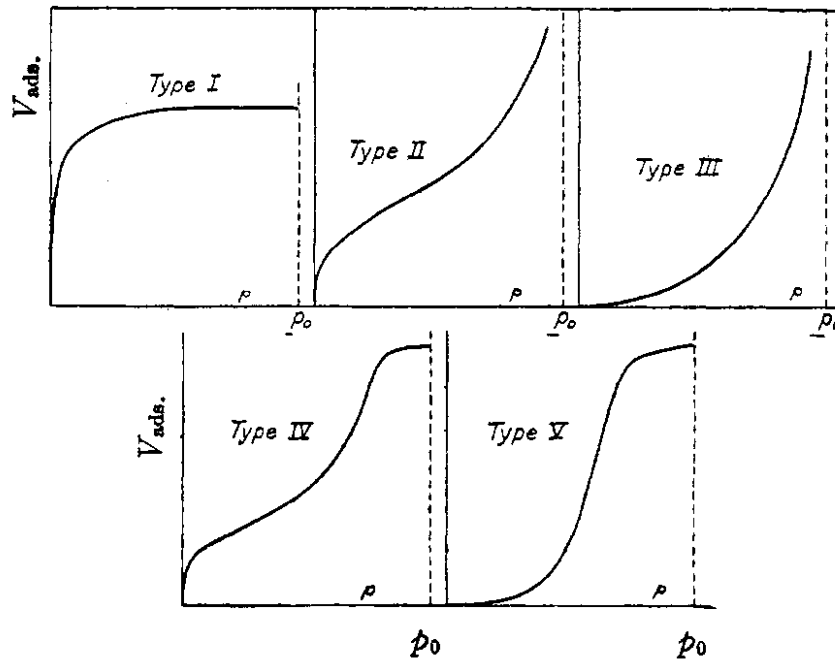


Figure 28: The five types of van der Waals Adsorption Isotherms [48].

Chapter 4: Conclusion

As in previous experiments measuring the Onsager heat of transport at the liquid-vapour interface, Q^* of *p*-tert-butyltoluene was found to be large and negative. However, the average value obtained for the heat of transport for this compound was much larger than expected at $-55 \pm 11 \text{ kJ mol}^{-1}$. Generally, when dealing with $|Q^*|$ outside the Knudsen layer the magnitude has tended to be only a significant portion of the latent heat of vaporisation, typically about half, and within the Knudsen zone $|Q^*|$ has tended to increase towards the latent heat of vaporisation as n_λ tends to zero. However, these results gave $|Q^*|$ values of approximately the same magnitude as ΔH_{vap} when well outside the Knudsen zone. Another notable difference between this experiment and previous systems was the behaviour of the pressure when decreasing the temperature gradient. These results show deviations from linearity, particularly at the larger ΔT values. This contrasts with experiments where ΔT was increased which gave linear plots and enabled the calculation of Q^* .

The non-linearity observed in plots of P against ΔT has been attributed to gas-kinetic temperature jumps at the surface of the upper plate. Values for the temperature jumps, temperature jump coefficients and thermal accommodation coefficients were calculated. Plots of the thermal accommodation coefficients against the temperature of the upper plate have also revealed the importance of the temperature difference between the two plates in determining the value of α .

Plots of the fractional surface coverage against P/P^0 revealed that the results for both *p*-tert-butyltoluene and water follow the BET isotherm. The non-linearity and shape of the plots obtained when using the original BET linearisation indicates they probably fit to a type III isotherm. Additional plots revealed that the c parameter is not a constant and resulted in the plots shown in Figure 27.

As yet, there are no published values of Q^* for CO₂ vapour at the surface of water. This experiment was one of a series of preliminary experiments leading up to the measurement of Q^* for CO₂ over water, which is a much more involved experiment. Results for the N₂O experiments were scattered and could not be presented in this project. These experiments will resume with the arrival of the new diode. Measuring Q^* for N₂O over water would be a significant step towards the CO₂ experiment. In order to calculate accurate fluxes of CO₂ from the oceans these values of Q^* must be known.

Future work with *p*-tert-butyltoluene could be carried out to investigate the discrepancies in the results obtained when starting at large ΔT values. The N₂O experiments will provide an insight into the temperature profile of the vapour. This will determine the correctness or otherwise of the temperature jump theory. This could also be done with N₂O over *p*-tert-butyltoluene to ascertain what temperature gradient the vapour is actually subject to when the experiment is started at large ΔT values. Once results have been successfully obtained for N₂O vapour over water, work can finally begin on the experiments with CO₂ vapour over water.

References

1. *Carbon dioxide chemistry: Environmental issues*, ed. J. Paul and C.M. Pradier. 1994, Stockholm: Athenaenum Press Ltd.
2. *The carbon cycle*, ed. T.M.L. Wigley and D.S. Schimel. 2000, Cambridge: Cambridge University Press.
3. Revelle, R. and H.E. Suess, *Carbon dioxide exchange between atmosphere and ocean and the question of an increase of atmospheric carbon dioxide during the past decades*. Bull. Scripps Inst. Oceanog. Univ. Calif., 1958: p. 2-11.
4. Watson, A.J. and J.C. Orr, *Carbon Dioxide Fluxes in the Global Ocean*, in *Ocean Biogeochemistry: the Role of the Ocean Carbon Cycle in Global Change (a JGOFS synthesis)*, M. Fasham, et al., Editors. 2003, Springer: Berlin. p. 123-141.
5. JGOFS, *The Joint Global Ocean Flux Study*, <http://www.uib.no/jgofs/jgofs.html>. 2004.
6. Orr, J.C., V.J. Fabry, O. Aumont, L. Bopp, S.C. Doney, R.A. Feely, A. Gnanadesikan, N. Gruber, A. Ishida, F. Joos, R.M. Key, K. Lindsay, E. Maier-Reimer, R. Matear, M. Patrick, A. Mouchet, R.G. Najjar, G.-K. Plattner, K.B. Rodgers, C.L. Sabine, J.L. Sarmiento, R. Schlitzer, R.D. Slater, I.J. Totterdell, M.-F. Weirig, Y. Yamanaka, and A. Yool, *Anthropogenic ocean acidification over the twenty-first century and its impact on calcifying organisms*. Nature (London, United Kingdom), 2005. **437**(7059): p. 681-686.
7. McGillis, W.R., Edson, J. B., Hare, J. E., Fairall, C. W., *Direct covariance air-sea CO₂ fluxes*. J. Geophys. Res., 2001. **106**(C8): p. 16,729-16,745.
8. GESAMP, *The Joint Group of Experts on the Scientific Aspects of Marine Environmental Protection*, <http://gesamp.imo.org/index.htm>. 2001.
9. Watson, A.J., R.C. Upstill-Goddard, and P.S. Liss, *Air-sea gas exchange in rough and stormy seas measured by a dual-tracer technique*. Nature, 1991. **349**: p. 145-147.
10. Jean-Baptiste, P. and A. Poisson, *Gas transfer experiment on a lake (Kerguelen Islands) using ³He and SF₆*. Journal of Geophysical Research, 2000. **105**(C1): p. 1177-1186.

11. Phillips, L.F., *CO₂ transfer at the air-sea interface: Numerical tests of the dual-tracer method*. Geophys. Res. Lett., 1995. **22**(19): p. 2597-2600.
12. Slanina, S., Vermeulen, A., De Wild, P., Wyers, G. P., *Instrumentation for Gas Exchange Measurements*, in *The Chemistry of the Atmosphere: Its Impact on Global Change*, J.G. Calvert, Editor. 1994, Blackwell Scientific Publications.
13. McGillis, W.R., Edson, J. B., Ware, J. D., Dacey, J. W. H., Hare, J. E., Fairall, C. W., Wanninkof, R., *Carbon dioxide flux techniques performed during GasEx-98*. Marine Chemistry, 2001. **75**: p. 267-280.
14. Iwata, T., Yoshikawa, Keiko, Nishimura, Katsutoshi, Higuchi, Yoshihisa, Yamashita, Takao, Kato, Shigeru, Ohtaki, Eiji, *CO₂ flux measurements over the sea surface by eddy correlation and aerodynamic techniques*. Journal of Oceanography, 2004. **60**(6): p. 995-1000.
15. Duce, R.A. and P.S. Liss, eds. *The sea surface and global change*. 1997, Cambridge University Press: Cambridge. 519.
16. Phillips, L.F., *CO₂ Transport at the Air-Sea Interface: Effect of Coupling of Heat and Matter Fluxes*. Geophys. Res. Lett., 1991. **18**(7): p. 1221-1224.
17. Jacobs, C., Nightingale, P., Upstill-Goddard, R. C., Friss Kjeld, J., Larson, S., Oost, W., *Comparison of the deliberate tracer method and eddy covariance measurements to determine the air/sea transfer velocity of CO₂*. Geophysical Monograph, 2002. **127**: p. 225-231.
18. Phillips, L.F., *Steady-state Heat and Matter Exchange at a Phase Interface*. J. Chem. Soc. Faraday Trans., 1991. **87**(14): p. 2187-2191.
19. Phillips, L.F., *CO₂ Transport at the Air-Sea Interface: Numerical Calculations for a Surface Renewal Model with Coupled Fluxes*. Geophys. Res. Lett., 1992. **19**(16): p. 1667-1670.
20. Phillips, L.F., *Experimental demonstration of Coupling of heat and matter fluxes at a gas-water interface*. J. Geophys. Res., 1994. **99**(D9): p. 18,577-18,584.
21. Phillips, L.F., *Steady-state thermodynamics of transfer through a gas-liquid interface, treated as a limiting case of thermo-osmosis*. Chem. Phys. Lett., 1994. **228**: p. 533-538.

22. Doney, S.C., *Irreversible Thermodynamic Coupling between Heat and Matter Fluxes across a Gas/Liquid Interface*. J. Chem. Soc. Faraday Trans., 1994. **90**(13): p. 1865-1874.
23. Mills, C.T. and L.F. Phillips, *Onsager heat of transport at the aniline liquid-vapour interface*. Chem. Phys. Lett., 2002. **366**: p. 279-283.
24. Denbigh, K.G., *The Thermodynamics of the Steady State*. Monographs on Chemical Subjects, ed. Methuen. 1951, London: Methuen & Co. Ltd. 103.
25. Denbigh, K.G. and G. Raumann, *The thermo-osmosis of gases through a membrane. I. Theoretical*. Proc. R. Soc. London, 1952. **210**(Ser. A): p. 377-387.
26. Alexander, K.F. and K. Wirtz, *Thermal osmosis in aqueous systems*. Z. physik. Chem., 1950. **195**: p. 165-74.
27. James, R.A. and L.F. Phillips, *Onsager heat of transport for water vapour at the surface of sulfuric acid*. Chem. Phys. Lett., 2005. **407**(4-6): p. 358-361.
28. James, R.A. and L.F. Phillips, *Onsager heat of transport for water vapour at the surface of glycerol-water mixtures*. Chem. Phys. Lett., 2006. **425**: p. 49-52.
29. Mills, C.T., Bones, David L., Casavecchia, Piergiorgio, Phillips, Leon F., *Onsager Heat of Transport Measured at the n-Heptanol Liquid-Vapor Interface*. Journal of Physical Chemistry B, 2004. **108**(8): p. 2681-2685.
30. Pursell, C.J. and L.F. Phillips, *Onsager heat of transport for water vapour at the surface of water and ice: thermal accommodation coefficients for water vapour on a stainless-steel surface*. Physical Chemistry Chemical Physics, 2006. **8**(40): p. 4694-4699.
31. Phillips, L.F., *The role of the air-sea temperature difference in air-sea exchange*. Geophys. Res. Lett., 2004. **31**(L137301): p. 1-4.
32. Mills, C.T., Bones, D.L., Casavecchia, P., Phillips, L.F., *Onsager heat of transport measured at the n-heptanol liquid-vapour layer*. J. Phys. Chem., 2004. **108**: p. 2681-2685.
33. Lockerby, D.A., J.M. Reese, and M.A. Gallis, *The usefulness of higher-order constitutive relations for describing the Knudsen layer*. Physics of Fluids, 2005. **17**(10): p. 100609/1-100609/6.

34. James, R.A., C.J. Pursell, and L.F. Phillips, *Pressure independence of the Onsager heat of transport for a gas-liquid interface at high pressures*. Chem. Phys. Lett., 2006. **To be published**.
35. James, R.A., *Onsager Heat of Transport at the Liquid-Vapour Interface of Glycerol-Water Solutions*, in *Chemistry Department*. 2006, University of Canterbury: Christchurch.
36. Mills, C.T. and L.F. Philips, *Distillation of a cool liquid onto a warmer surface*. Chem. Phys. Lett., 2003. **372**(5-6): p. 615-619.
37. McCormick, N.J., *Gas-surface accommodation coefficients from viscous slip and temperature jump coefficients*. Physics of Fluids, 2005. **17**(10): p. 107104/1-107104/8.
38. Payne, H., *Temperature jump and velocity of slip at the boundary of a gas*. Journal of Chemical Physics, 1953. **21**: p. 2127-31.
39. Cercignani, C., *Mathematical Methods in Kinetic Theory*. 1969, New York: Plenum Press.
40. Li, Y.Q., P. Davidovits, Q. Shi, J.T. Jayne, C.E. Kolb, and D.R. Worsnop, *Mass and thermal accommodation coefficients of H₂O(g) on liquid water as a function of temperature*. Abstracts of Papers, 222nd ACS National Meeting, Chicago, IL, United States, August 26-30, 2001, 2001: p. PHYS-138.
41. Atkins, P.W., *Physical Chemistry*. 4th ed. 1990, Oxford: Oxford University Press.
42. Cox, J.D. and R.J.L. Andon, *Second virial coefficients of pyridine and benzene and some methyl homologs between 135 Deg and 165 Deg*. Transactions of the Faraday Society, 1958. **54**: p. 1622-9.
43. Lide, D.R., ed. *CRC Handbook of Chemistry and Physics*. 73 ed. 1992, Chemical Rubber Publishing Company: Florida.
44. Loyalka, S.K., Siewert, C. E., Thomas, Jr., J. R., *Temperature-jump problem with arbitrary accommodation*. Phys. Fluids, 1978. **21**(5).
45. Salvador, F., C. Sanchez-Jimenez, M.J. Sanchez-Montero, and A. Salvador, *A review of the application of the BET equation to experimental data. The C parameter*. Studies in Surface Science and Catalysis, 2002. **144**(Characterization of Porous Solids VI): p. 379-386.

46. Sanchez-Montero, M.J., C. Herdes, F. Salvador, and L.F. Vega, *New insights into the adsorption isotherm interpretation by a coupled molecular simulation-experimental procedure*. Applied Surface Science, 2005. **252**(3): p. 519-528.
47. Reilly, J., Rae, W. N., *Physico-Chemical Methods*. 5th ed. Vol. 1. 1954, London: Methuen & Co. Ltd.
48. Brunauer, S., L.S. Deming, W.E. Deming, and E. Teller, *A theory of the van der Waals adsorption of gases*. Journal of the American Chemical Society, 1940. **62**: p. 1723-32.